12-2016

Landsat 5 Thematic Mapper Reflectance and NDVI 27-year Time Series Inconsistencies Due to Satellite Orbit Change

Hankui Zhang
South Dakota State University, hankui.zhang@sdstate.edu

David P. Roy
South Dakota State University, david.roy@sdstate.edu

Remote Sensing of Environment 186 (2016) 217–233

Contents lists available at ScienceDirect

Remote Sensing of Environment

journal homepage: www.elsevier.com/locate/rse

Landsat 5 Thematic Mapper reflectance and NDVI 27-year time series inconsistencies due to satellite orbit change

H.K. Zhang *, D.P. Roy

Geospatial Sciences Center of Excellence, South Dakota State University, Brookings, SD 57007, USA

ARTICLE INFO

Article history:
Received 26 February 2016
Received in revised form 27 June 2016
Accepted 11 August 2016
Available online 24 August 2016

Keywords:
Landsat 5
Long term data record
Orbit drift
Solar zenith variation
BRDF

ABSTRACT

The Landsat 5 Thematic Mapper (TM) sensor provided the longest single mission terrestrial remote sensing data record but temporally sparse station keeping maneuvers meant that the Landsat 5 orbit changed over the 27 year mission life. Long-term Landsat 5 TM reflectance inconsistencies may be introduced by orbit change induced solar zenith variations combined with surface reflectance anisotropy, commonly described by the Bi-directional Reflectance Distribution Function (BRDF). This study quantifies the local overpass time and observed solar zenith angle changes for all the Landsat 5 TM images available at two latitudinally separated locations along the same north-south Landsat path (27) in Minnesota (row 26) and Texas (row 42). Over the 27 years the Landsat 5 orbit changed by nearly 1 h and resulted in changes in the Landsat 5 observed solar zenith angle of >10°. The Landsat 5 orbit was relatively stable from 1984 to 1994 and from 2007 to 2011, but changed rapidly from 1995 to 2000, and from 2003 to 2007. Rather than directly examine Landsat 5 TM reflectance time series a modelling approach was used. This was necessary because unambiguous separation of orbit change induced Landsat reflectance variations from other temporal variations is non-trivial. The impact of Landsat 5 orbit induced observed solar zenith angle variations on the red and near-infrared reflectance and derived normalized difference vegetation index (NDVI) values were modelled with respect to different Moderate-Resolution Imaging Spectroradiometer (MODIS) BRDF land cover types. Synthetic nadir BRDF-adjusted reflectance (NBAR) for the Landsat 5 TM observed and a modelled reference year 2011 solar zenith were compared over the 27 years of acquisitions. Ordinary least squares linear regression fits of the NBAR difference values as a function of the acquisition date indicated an increasing trend in red and near-infrared NBAR and a decreasing trend in NDVI NBAR due to orbit changes. The trends are statistically significant but small, no more than 0.0006 NDVI/year. Comparison of certain years of Landsat 5 data may result in significant reflectance and NDVI differences due only to Landsat 5 orbit changes and cause spurious detection of "browning" vegetation events and underestimation of greening trends. The greatest differences will occur when 1995 Landsat 5 TM data are compared with 2007 to 2011 data; NDVI values could be up to 0.11 greater in 1995 than in 2011 for anisotropic land cover types and up to 0.05 greater for average CONUS land cover types. A smaller number of Landsat 5 TM images were also examined and provide support for the modelled based findings. The paper concludes with a discussion of the implications of the research findings for Landsat 5 TM time series analyses.

1. Introduction

The Landsat 5 satellite, carrying the Thematic Mapper (TM) and Multispectral Scanner (MSS) sensors, provided the longest operating Earth remote sensing satellite mission in history. Landsat 5 was launched in March 1984 into an approximately 710 km sun-synchronous polar orbit and was decommissioned in June 2013. The need for consistent Landsat time series is well established and the nearly three decades of Landsat 5 TM data are sufficiently resolved to enable chronicling of anthropogenic and natural change in an era when climate change has become evident (Roy et al., 2014). Considerable effort was expended on ensuring a reliable and consistently calibrated Landsat TM 5 data record (Markham and Helder, 2012) and for many parts of the world, particularly the United States, the geolocation of Landsat 5 data was well characterized and stable (Storey and Choate, 2004). Over the mission life of a polar orbiting satellite the orbit altitude and inclination may drift due to a number of factors, predominantly gravitational ones, and station keeping maneuvers (orbit burns) are needed to maintain the orbit (Wertz, 2001). Unfortunately, irregular station keeping maneuvers meant that the Landsat 5 orbit drifted more than usual and so the solar illumination geometry changed. This is a concern

* Corresponding author.
E-mail address: hankui.zhang@sdstate.edu (H.K. Zhang).

http://dx.doi.org/10.1016/j.rse.2016.08.022

as we demonstrate in this paper that the orbit changes may result in the spurious detection of surface changes, or conversely masking of surface changes, observed in Landsat 5 TM reflectance time series.

The majority of terrestrial surfaces reflect optical wavelength radiation anisotropically with a directional dependence that varies as a function of the sun–target–sensor geometry, commonly described by the Bi-directional Reflectance Distribution Function (BRDF). The BRDF is controlled by several factors including the type, amount, structure and spacing of the vegetation and the background soil reflectance. Typically, the BRDF of terrestrial surfaces can be described by dome or bowl anisotropic reflectance shapes with a retro-reflectance peak (hot spot) (Jackson et al., 1990; Li and Strahler, 1992; Roujean et al., 1992; Rahman et al., 1993; Pinty et al., 2002). The Landsat acquisition view zenith angle is usually less than the solar zenith angle and so Landsat reflectance hot-spot effects do not occur (Zhang et al., 2016). For a nadir view the red reflectance usually decreases with increasing solar zenith because the direct solar irradiance enters the vegetation canopy more obliquely and so has a higher probability of interacting with foliage elements and because of increased shadow effects; whereas, the near-infrared (NIR) reflectance may not increase due to multiple-scattering within the canopy and if the soil reflectance is lower than the vegetation reflectance (Chen and Leblanc, 2001; Privette et al., 1997). Spectral band ratio based vegetation indices, such as the commonly used normalized difference vegetation index (NDVI), typically have less sensitivity to view and solar geometry variations than the red and NIR reflectance, although the nadir view NDVI usually increases with solar zenith (Huete, 1987; Goward and Huemmrich, 1992; Pinter, 1993; Deering et al., 1994; Epiphanio and Huete, 1995; Leblanc et al., 1997; McDonald et al., 1998; Gao et al., 2002; Ishihara et al., 2015).

Directional reflectance artifacts will be introduced over non-lambertian surfaces if the orbit of a sun-synchronous satellite changes and the local overpass time, and so observed solar zenith angle, change. The impact of orbit drift on reflectance time series from sun-synchronous satellite sensors has been examined in particular with respect to the Advanced Very High Resolution Radiometer (AVHRR) sensors that have well documented orbit drifts that changed the solar observation geometry and so retrieved reflectance over the sensor mission life (Privette et al., 1995; Kaufmann et al., 2000; Tucker et al., 2005). The impact of solar variations on Landsat directional reflectance was considered by Nagol et al. (2015) who estimated relative red and near-infrared reflectance reductions of >30% between the peak and the end of the growing season at mid-latitudes. Recently, BRDF effects due to the change in the Landsat 5 orbit were analyzed using a BRDF model parameterized with field and airborne directional reflectance measurements of different land covers (Gao et al., 2014). The Gao et al. (2014) study found that changes in the Landsat 5 orbit were greatest in the mid-1990s and resulted in a modelled change in nadir view reflectance of about 0.01–0.02 in the Landsat 5 TM red and NIR bands respectively. However, no detailed quantification of Landsat 5 orbit changes considering the over pass time and solar zenith angles, or study of the impact of these changes on the temporal consistency of Landsat 5 reflectance and NDVI time series, has been undertaken.

This paper quantifies the orbital changes present in the 27 year Landsat 5 TM record in terms of the nadir overpass time and solar zenith angle, and examines if the changes have significant impact on red, NIR, and NDVI time series. The nadir solar zenith angle and local overpass time at the center of every available Landsat 5 TM acquisition at two latitudinally separated locations are examined. A modelling approach is used as differentiation of orbit change induced reflectance time series effects from seasonal and land cover surface changes, and from other factors such as residual atmospheric and cloud contamination, is complex. Twenty seven years of Landsat 5 solar zenith and acquisition time metadata information are used in conjunction with Moderate Resolution Imaging Spectroradiometer (MODIS) BRDF spectral model parameters to estimate the nadir BRDF-adjusted reflectance (NBAR) for the observed solar zeniths and a modelled reference year 2011 solar zenith. Fixed BRDF spectral model parameters, defined by examination of a year of conterminous United States (CONUS) MODIS BRDF product values and for different CONUS land covers, are considered to quantify orbit drift induced reflectance changes over typical CONUS surfaces. The reported BRDF modelling results are expected to be quite conservative as there is a significant scale difference between Landsat 30 m and MODIS 500 m pixels. In addition, the fixed MODIS BRDF spectral model parameters are smoothed by taking the mean parameter values over twelve months. Therefore, it is likely that at Landsat 30 m resolution certain geographic locations and times will have greater reflectance anisotropy than captured by the fixed BRDF spectral model parameters and so a greater sensitivity to Landsat 5 TM orbit change. To gain more confidence and insights into the BRDF modelling results actual 30 m pixel reflectance and NDVI extracted from a small number of example Landsat 5 TM images are compared with the acquisition solar zenith.

The paper is structured as follows. First the Landsat 5 TM orbit geometry and then the Landsat 5 TM metadata and MODIS BRDF and land cover product data, and the example Landsat 5 TM images are described. This is followed by description of the Landsat 5 overpass time calculation, including the models used to derive reference year 2011 overpass times and solar zeniths, and then the MODIS based NBAR modelling approach. The results are followed by concluding remarks that include a discussion of the implications of the research findings for Landsat 5 TM time series analyses.

2. Data

2.1. Landsat 5 TM orbit characteristics

Satellites in polar circular sun-synchronous orbits, such as Landsat 5, have an inclination and altitude configured so that the local overpass time is approximately the same each time the satellite passes overhead (Wertz, 2001, Ignatov et al., 2004). Landsat 5 was launched in 1984 into a 705 km polar orbit with a 98.2° inclination that provided a sun-synchronous orbit with a Mean Local Time of Descending Node (MLTDN) (i.e., mean sunlit equatorial north to south crossing time) of 9:45 a.m. (Hassett and Johnson, 1984). This was the same as the Landsat 4 orbit but was phased to ensure a combined Landsat 4 and 5 8-day full Earth coverage cycle. Initially the Landsat 5 orbit was maintained by periodic station keeping maneuvers to maintain the ground track and orbit phase with Landsat 4, and the MLTDN was required to not vary by more than ± 15 min from 9:45 a.m. (Hassett and Johnson, 1984). Unfortunately, the Landsat 5 orbit was not maintained consistently. This was due to the unforeseen longevity of the Landsat 5 mission, and to the different federal agency and commercial company operators over the mission life (Goward et al., 2006). In particular, there were fewer station keeping maneuvers undertaken in the mid 1990s when Landsat 5 was operated commercially, and then after the return of Landsat 5 operations to the Federal government more routine orbit maintenance was resumed to ensure a combined 8-day full Earth coverage cycle with Landsat 7 (launched in 1999) and to reflect the needs of the increasingly occupied 705 km polar orbit space (Levi and Palmer, 2011; Vincent, 2012; Goward et al., 2016).

2.2. Landsat 5 TM metadata used

The Landsat 5 TM acquired 30 m pixel reflective wavelength observations from March 1984 until November 2011. The Landsat 5 TM data are available in approximately 180 km × 170 km scenes defined in a Worldwide Reference System (WRS) of path (ground track parallel) and row (latitude parallel) coordinates with associated descriptive metadata (Arvidson et al., 2006). The global Landsat data are held at the United States Geological Survey (USGS) Earth Resources Observation and Science (EROS) Center and the archived Landsat 5 TM data have variable acquisition coverage (Kovalskyy and Roy, 2013; Wulder

et al., 2016). This is primarily because the Landsat 5 data were acquired with no systematic global acquisition plan, reflecting the different federal agency and commercial operators, and also different international ground station collections, and several technical down-link transmission issues that occurred later in the Landsat 5 mission life (Goward et al., 2006; Chander et al., 2007; Loveland and Dwyer, 2012).

The metadata, not the images, for every available day time Landsat 5 TM acquisition in the U.S. Landsat archive over path/row 27/26 (centered on 91.9363°W 48.8687°N, Minnesota) and 27/42 (centered on 98.9661°W 26.0011°N, Texas) were used (henceforth referred to for brevity, as Minnesota and Texas). These two locations were selected because they fall within the CONUS, which globally has the richest temporal Landsat 5 TM data collection (Wulder et al., 2016), and because they are on the same Landsat orbit path but span a large latitudinal range. Locations with different latitudes are of interest because nominally the Landsat local overpass time changes only with latitude and because the solar zenith angle for a given local time changes with latitude (Zhang et al., 2016).

The following metadata for all the available Minnesota and Texas Landsat 5 acquisitions were used: "sceneStartTime", "sceneStopTime", "sunElevation", "sceneCenterLatitude", and "sceneCenterLongitude". These metadata and their use are described in more detail in Section 3. In 1984 and 1985 seven acquisitions had "sunElevation" metadata values that were defined imprecisely ($\pm 0.5°$ precision) and so the metadata for those acquisitions were discarded. The metadata for a total of 567 (Minnesota) and 447 (Texas) acquisitions sensed from March 16, 1984 to November 14, 2011 were used in this study.

2.3. MODIS land cover product

The Collection 5 annual 500 m MODIS land cover product (MCD12Q1) (Friedl et al., 2010) for 2010 was used to define land cover information for the Landsat 5 TM NBAR modelling analysis. The MCD12Q1 International Geosphere-Biosphere Program (IGBP) classification scheme, which classifies each 500 m pixel into one of 17 classes and has a reported 75% overall land cover classification accuracy (Friedl et al., 2010) was used. The MCD12Q1 product is defined in $10° \times 10°$ MODIS Land tiles defined in the equal area sinusoidal projection (Wolfe et al., 1998), a total of 11 tiles covering the CONUS were used.

2.4. MODIS BRDF/Albedo product

The 500 m Collection 5 MCD43A1 and MCD43A2 MODIS BRDF spectral model parameter product suite was used (Schaaf et al., 2011). These products define Ross-Thick/Li-Sparse-Reciprocal BRDF spectral model parameters (determined as those that best fit all of the cloud-cleared, atmospherically-corrected MODIS Terra and Aqua reflectance values observed at each gridded 500 m pixel location over a 16 day period) and associated per pixel quality information. The Ross-Thick/Li-Sparse-Reciprocal BRDF model defines reflectance as a weighted sum of an isotropic parameter and two functions (or kernels) of viewing and illumination geometry (Roujean et al., 1992), where one kernel is derived from radiative transfer models (Ross, 1981) and the other is based on surface scattering and geometric shadow casting theory (Li and Strahler, 1992). The products are used to compute the directional reflectance at any desired viewing and solar geometry as:

$$\rho\ (\lambda_{MODIS}\ ,\Omega,\ \ \Omega') = f_{iso}(\lambda_{MODIS}) + f_{vol}(\lambda_{MODIS})\ K_{vol}(\Omega,\Omega') + f_{geo}(\lambda_{MODIS})\ K_{geo}(\Omega,\Omega'). \quad (1)$$

where $\rho\ (\lambda_{MODIS},\Omega,\ \ \Omega')$ is the MODIS spectral reflectance for wavelength λ_{MODIS}, for viewing vector Ω (view zenith and azimuth angles) and solar illumination vector Ω' (solar zenith and azimuth angles), $K_{vol}(\Omega,\Omega')$ and $K_{geo}(\Omega,\Omega')$ are the volumetric scattering and geometic-optical model kernels respectively which depend only on the sun-view geometry (Ω,Ω'), and $f_{iso}(\lambda_{MODIS})$, $f_{vol}(\lambda_{MODIS})$, and $f_{geo}(\lambda_{MODIS})$ are the spectral BRDF model parameters (Schaaf et al., 2002).

The MODIS BRDF/Albedo quality product (MCD43A2) was used to remove all but the highest quality spectral BRDF model parameter 500 m pixel values (Ju et al., 2010). In addition, only snow-free parameters as labeled in the MCD43A2 product were used. All of the MODIS MCD43A1 and MCD43A2 products for 2010 over the CONUS were used. This corresponded to a total of 11 MODIS Land $10° \times 10°$ product tiles defined every 8-days for all of 2010.

2.5. Example Landsat 5 TM images

In this study a modelling approach (Section 3) was used to investigate Landsat 5 TM orbit change induced reflectance change rather than direct examination of Landsat 5 TM reflectance. This is because reliable identification of locations that have remained unchanged over the Landsat 5 mission life, and have not been subject to gradual or abrupt land cover and surface condition changes (Vogelmann et al., 2012; McManus et al., 2012; Melaas et al., 2013; Sexton et al., 2013; Gray and Song, 2013; Boschetti et al., 2015), is non-trivial. In addition, even for an "unchanged" location, seasonal and inter-annual variations in the surface state (e.g., soil moisture and vegetation condition changes) may be conflated with orbit change induced reflectance effects. Conventionally, seasonal variations in the surface state and the position of the sun mean that anniversary date Landsat images are compared for time series analyses. However, anniversary date images are not always available or cloud-free. Landsat time series analyses are complicated further by factors including sensor saturation, residual cloud and atmospheric contamination and shadows that perturb retrieved surface reflectance (Roy et al., 2016a).

Despite these limitations, a small number of example Landsat images were examined. Landsat 5 TM L1T cloud-free summer anniversary date images sensed over Crater Lake National Park, Oregon (WRS-2 path/row 45/30) acquired on September 2, 1991, August 28, 1995, August 30, 1996, September 2, 1997, September 5, 1998, August 28, 2001, August 31, 2002, September 5, 2004, August 29, 2007, August 31, 2008, September 3, 2009, and September 6, 2010, were examined. Three 3×3 30 m pixel subsets were extracted from each image over sites that are described in Vogelmann et al. (2016). The sites are over pumice desert that had largely unchanged Landsat NDVI and two coniferous forest areas that had only gradual NDVI increases and decreases. The Landsat 5 TM L1T images were converted to top of atmosphere reflectance and then atmospherically corrected to surface reflectance using the Landsat Ecosystem Disturbance Adaptive Processing System (LEDAPS) code (Masek et al., 2006). Two per-pixel cloud masks were used, the heritage Landsat project automatic cloud cover assessment algorithm (ACCA) (Irish et al., 2006) and a decision tree cloud mask algorithm that generally performs better than ACCA for Landsat 7 ETM+ over the CONUS (Roy et al., 2010). The pre-processed Landsat data were projected with nearest neighbor resampling into fixed geolocated tiles in the MODIS sinusoidal equal area projection using the Web Enabled Landsat Data (WELD) processing software (Roy et al., 2010) so that they could be compared through time. Only cloud-free and unsaturated pixel values were considered.

3. Analysis methodology

3.1. Landsat 5 TM acquisition local overpass time and solar zenith derivation

The solar zenith angle and local overpass time at nadir at the center of each Landsat 5 TM acquisition were taken from the metadata. The

solar zenith angle is the angle subtended between the sun and the local normal to the earth's surface, derived as:

$$\theta_{observed} = 90° - \text{sunElevation} \quad (2)$$

where $\theta_{observed}$ is the solar zenith angle at the center of the acquisition and "sunElevation" is the acquisition center solar elevation metadata value. For a given day of the year the solar zenith angle at Landsat nadir is approximately the same along a line of latitude but the solar zenith changes over the year with the seasonal progression of the position of the sun in the sky (Blanco-Muriel et al., 2001; Ignatov et al., 2004; Zhang et al., 2016).

The local overpass time was derived from the Landsat metadata in the same way as described in Zhang et al. (2016) as:

$$t_{local} = \begin{cases} t_{UTC} + \lambda/15 + 24 & if\ (t_{UTC} + \lambda/15) < 0 \\ t_{UTC} + \lambda/15 & if\ 0 \leqslant (t_{UTC} + \lambda/15) \leqslant 24 \\ t_{UTC} + \lambda/15 - 24 & if\ (t_{UTC} + \lambda/15) > 24 \end{cases} \quad (3)$$

where t_{local} is the local overpass time (decimal 24-hour units), t_{UTC} is the Coordinated Universal Time (UTC) of the acquisition center derived as the mean of the two "sceneStartTime" and "sceneStopTime" metadata values for each acquisition, and λ is the acquisition center longitude stored in the "sceneCenterLongitude" metadata. The "sceneStartTime" and "sceneStopTime" metadata values define the UTC time with a precision of five decimal places, and also include the year, and the day of the year (1 to 365 or 366) of the acquisition.

3.2. Landsat 5 TM year 2011 reference local overpass time and solar zenith derivation

The following model of the Landsat overpass time for global climate year 2011 (December 2010 to November 2011) was used to provide a reference benchmark to compare the 27 years of overpass times against:

$$\begin{aligned} t_{reference} = {} & 1.36292 \times 10^{-9}\alpha^5 - 3.15403 \times 10^{-8}\alpha^4 \\ & - 3.15819614 \times 10^{-6}\alpha^3 + 0.0000652685643\alpha^2 \\ & + 0.0120604786763\alpha + 10.06 \end{aligned} \quad (4)$$

where $t_{reference}$ is the reference modelled Landsat local overpass time for 2011 and α is the Landsat acquisition center latitude defined by the "sceneCenterLatitude" metadata value. The model was derived in a previous study (Zhang et al., 2016) by ordinary least squares regression ($r^2 = 0.988$, mean absolute error of 2.34 min) considering the local overpass time and latitudes of all the global non-Antarctic Landsat 5 TM and Landsat 7 ETM+ acquisitions in the Landsat U.S. archive for climate year 2011 (147,358 acquisitions for December 1, 2010 to November 30, 2011). Climate year 2011 was used because it is the last year of the Landsat 5 TM data record, and in that year the Landsat 5 and 7 local overpass times were similar with a mean difference of 4.236 min (Zhang et al., 2016) and the orbit was relatively stable compared to previous years.

The solar zenith angle at $t_{reference}$, termed $\theta_{reference}$, was computed using an astronomical model parameterized with the Landsat acquisition center latitude, longitude, date (year and day of the year), and the $t_{reference}$ value, for each Texas and Minnesota acquisition. The astronomical model is described by Blanco-Muriel et al. (2001) and is sufficiently accurate for the purposes of this study with a reported average and standard deviation solar zenith prediction error of 0.001 and 0.114 min of arc.

3.3. Landsat 5 TM overpass time and solar zenith variation analysis

To examine the Landsat 5 satellite orbit drift, and the temporal occurrence of periodic station keeping maneuvers, the 27 years of local overpass times (t_{local}) and 2011 reference times ($t_{reference}$) were plotted and summary statistics (mean, standard deviation, and range) were computed independently for the Texas and Minnesota data.

To examine the seasonal variation of the observed solar zenith angle, and the impact of the Landsat 5 satellite drift, the $\theta_{observed}$ and ($\theta_{observed} - \theta_{reference}$) was plotted for 1985, 1990, 1995, 2000, 2005, and 2010. Summary statistics of the difference ($\theta_{observed} - \theta_{reference}$) were derived independently for each Landsat 5 TM acquisition over the 27 years of Texas and Minnesota data. The angles $\theta_{observed}$ and $\theta_{reference}$ should be similar in 2011 with only small differences due to the fifth degree polynomial fit error used to derive $t_{reference}$, in other years greater differences between $\theta_{observed}$ and $\theta_{reference}$ will be indicative of Landsat 5 orbit differences relative to year 2011. Conventional ordinary least squares (OLS) linear regression fits of the differences ($\theta_{observed} - \theta_{reference}$) as a function of the date of the Landsat acquisition were generated for the Texas and Minnesota data. The regression slopes were examined as they quantify the first-order solar zenith trend introduced by the Landsat 5 orbit drift. The goodness of fit of the OLS regressions were assessed by the coefficient of determination (r^2) and the significance of the OLS regressions assessed by examination of the regression overall F-statistic p-value.

3.4. Landsat 5 TM reflectance and NDVI time series modelling using a semi-empirical BRDF model

3.4.1. MODIS BRDF spectral model parameter derivation

A number of models have been developed to simulate reflectance and how it varies with the optical properties of the surface components and their structural variability and physical arrangement (Gobron et al., 1997; Jacquemoud et al., 2009; Disney et al., 2011; Yin et al., 2015). In this study however, as we are interested only in the change in surface reflectance due to solar geometry changes, an established semi-empirical BRDF model is sufficient. The Ross-Thick/Li-Sparse-Reciprocal BRDF spectral model was used to derive synthetic nadir BRDF-adjusted reflectance (NBAR) independently for the 27 years of Landsat 5 TM Texas and Minnesota data. To reduce reporting complexity, only the NBAR values for the red and near-infrared (NIR), and also the NDVI (derived as NIR minus red NBAR divided by their sum), were estimated. The red and NIR NBAR values were derived, as Eq. (1), setting the view zenith to 0° and setting the solar zenith angle to either $\theta_{observed}$ or to $\theta_{reference}$ and using fixed spectral BRDF model parameter values. Definition of the azimuthal angles is unimportant because at nadir view the reflectance is independent of the azimuthal geometry.

Fixed BRDF spectral model parameters were used so that only the effects of the Landsat 5 orbit drift on the solar zenith were modelled, i.e., surface temporal changes were not modelled. Average CONUS and also average CONUS land cover specific parameters were used as reflectance anisotropy is expected to be different among land cover classes (Barnsley et al., 1997; Roberts, 2001; Gao et al., 2003). The CONUS mean red and the mean NIR parameter values were derived from the MODIS MCD43 data considering only the highest quality snow-free CONUS MCD43 500 m pixel values defined every 16 days for 2010 as described in Roy et al. (2016b). Similarly, the mean 12 month red and NIR spectral BRDF model parameters for each of the MODIS land cover classes were derived. Any MCD43 pixels that were located where the corresponding 2010 MODIS land cover pixels were classified as snow and ice, permanent wetland, or water, were not considered. The snow and ice, permanent wetland, and water classes were not considered because BRDF inversion over snow covered surfaces and water may be less reliable (Schaaf et al., 2002, Roy et al., 2016b) and because wetlands are known to be classified unreliably (Friedl et al., 2010).

3.4.2. Landsat 5 TM NBAR reflectance and NDVI time series modelling

For each Landsat 5 TM acquisition, the red, NIR and NDVI NBAR values were derived for the $\theta_{observed}$ and for the $\theta_{reference}$ solar zenith angles; denoted $\rho_{red\ observed}$ and $\rho_{red\ reference}$, $\rho_{NIR\ observed}$ and $\rho_{NIR\ reference}$, and $NDVI_{observed}$ and $NDVI_{reference}$. Summary statistics of $\rho_{red\ observed}$ −

$\rho_{red\ reference}$, $\rho_{NIR\ observed} - \rho_{NIR\ reference}$, and $NDVI_{observed} - NDVI_{reference}$, were derived independently for the 27 years of Texas and Minnesota Landsat 5 TM data. Conventional OLS linear regression fits of the NBAR differences as a function of the date of the Landsat acquisition were generated and the regression slopes were examined as they quantify the first-order reflectance trend introduced by the Landsat 5 orbit drift. The goodness of fit of the OLS regressions were assessed by the coefficient of determination (r^2) and the significance of the OLS regressions assessed by examination of the regression overall F-statistic *p*-value. This analysis was undertaken independently using the NBAR values derived using the different sets of 12 month mean BRDF spectral model parameters.

4. Results

4.1. Landsat 5 TM local overpass time variation

Fig. 1 shows the 27 years of local overpass times (t_{local} in decimal 24-hour time) for the Minnesota and Texas data. There is an evident temporal pattern of increasing and then decreasing overpass times as the Landsat orbit was adjusted by periodic station keeping maneuvers. Over the 27 years the mean t_{local} was 10.3840 and 10.0535 h for Minnesota and Texas respectively (horizontal black lines, Fig. 1). The mean values are different between the two locations because t_{local} increases with latitude (Ignatov et al., 2004; Zhang et al., 2016). Importantly, and quite clearly, the local overpass time varied over the 27 years. In the mid-1990s there were evidently fewer station keeping maneuvers, this corresponded to the period when Landsat 5 was operated commercially, and the greatest Landsat 5 overpass time drifts occurred. The local overpass times increased after 2002 and reflected the Federal government's efforts to begin to adjust the Landsat 5 orbit to match that of Landsat 7. Over the 27 years the range (maximum minus minimum) and standard deviations of the overpass times were 0.9153 and 0.2110 h respectively (Minnesota) and 0.9174 and 0.2275 h respectively (Texas).

The illustrated reference modelled Landsat local overpass time for 2011 ($t_{reference}$) (red dots, Fig. 1) have 27 year mean values of 10.6367 and 10.3640 h for Minnesota and Texas respectively. The $t_{reference}$ values are derived only as a function of latitude (Eq. (4)) and so should be constant over the 27 years. However, there is a small temporal variation (maximum to minimum ranges of 0.0025 h and 0.0005 h for Minnesota and Texas respectively) due to latitudinal shifts in the Landsat path/row locations (Kovalskyy and Roy, 2013). This variation has no impact on solar zenith value differences computed as ($\theta_{observed} - \theta_{reference}$) that are examined in the following sections. Evidently, after 2005 the local overpass times are close to the $t_{reference}$ times; they are not exactly the same because the Landsat 5 orbit still drifted and because of the statistical fitting error used to derive Eq. (4) (mean absolute difference of 2.34 min) (Zhang et al., 2016).

4.2. Landsat 5 TM solar zenith angle variation

Fig. 2 (top) shows six example years (every five years since 1985) of $\theta_{observed}$ plotted as a function of the day of year of image acquisition for Minnesota (left) and Texas (right). The expected seasonal variation in $\theta_{observed}$ is apparent with the smallest solar zenith angles occurring in the northern hemisphere summer when the sun is most directly overhead at the time of Landsat overpass. The evident difference in $\theta_{observed}$ among the years is due predominantly to the Landsat 5 orbit drift. Over the 27 years (not plotted) the maximum and minimum $\theta_{observed}$ values occurred on December 20, 1995 (77.5731°) and June 12, 2007 (29.7330°) respectively for Minnesota and on January 5, 1996 (61.3363°) and May 27, 2007 (22.1039°) respectively for Texas.

Fig. 2 (bottom) shows the difference between the observed solar zenith and the modelled 2011 reference solar zenith. The greatest differences are >5° (Minnesota) and 10° (Texas). Among the illustrated years the differences are greatest for 1995 when t_{local} was particularly different from $t_{reference}$ (Fig. 1). The differences are greater for Texas than Minnesota because over a day the sun moves more rapidly across the sky (i.e., solar zenith angle changes more rapidly) at lower latitudes. Thus, the same $t_{local} - t_{reference}$ difference will result in greater $\theta_{observed} - \theta_{reference}$ differences at lower latitudes (i.e., Texas). The seasonal timing of the differences also varies among years and, for example, the greatest difference for year 2000 is in the spring and not in the summer as for the other illustrated years.

Fig. 3 shows the 27 year solar zenith angle differences ($\theta_{observed} - \theta_{reference}$) plotted as a function of the date of Landsat 5 TM image acquisition for Minnesota (top) and Texas (bottom). For visual reference the green dots show the Summer Landsat acquisitions. Summer is defined as the period spanning six weeks before and after June 21 when the summer solstice occurs. As observed in Fig. 2, the solar zenith angle differences exhibit a pronounced seasonal variation and in each year there are greater differences in summer than in winter. Over the 27 years the mean absolute differences were 1.3727° and 3.2328°, and the maximum differences were 5.8885° (occurring on July 13, 1995) and 11.2415° (July 29, 1995), for Minnesota and Texas respectively.

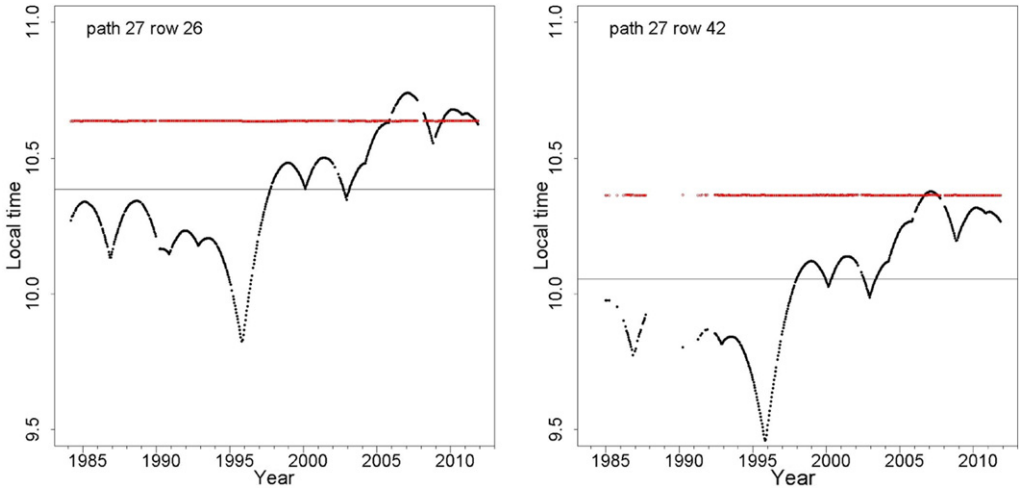

Fig. 1. 27 years of Landsat 5 TM local overpass times (t_{local} Eq. (3)) (black dots) and 2011 reference overpass times ($t_{reference}$ Eq. (4)) (red dots) for Minnesota (path/row 27/26, left) and Texas (path/row 27/42, right). The 27 year mean t_{local} is shown by the horizontal black lines.

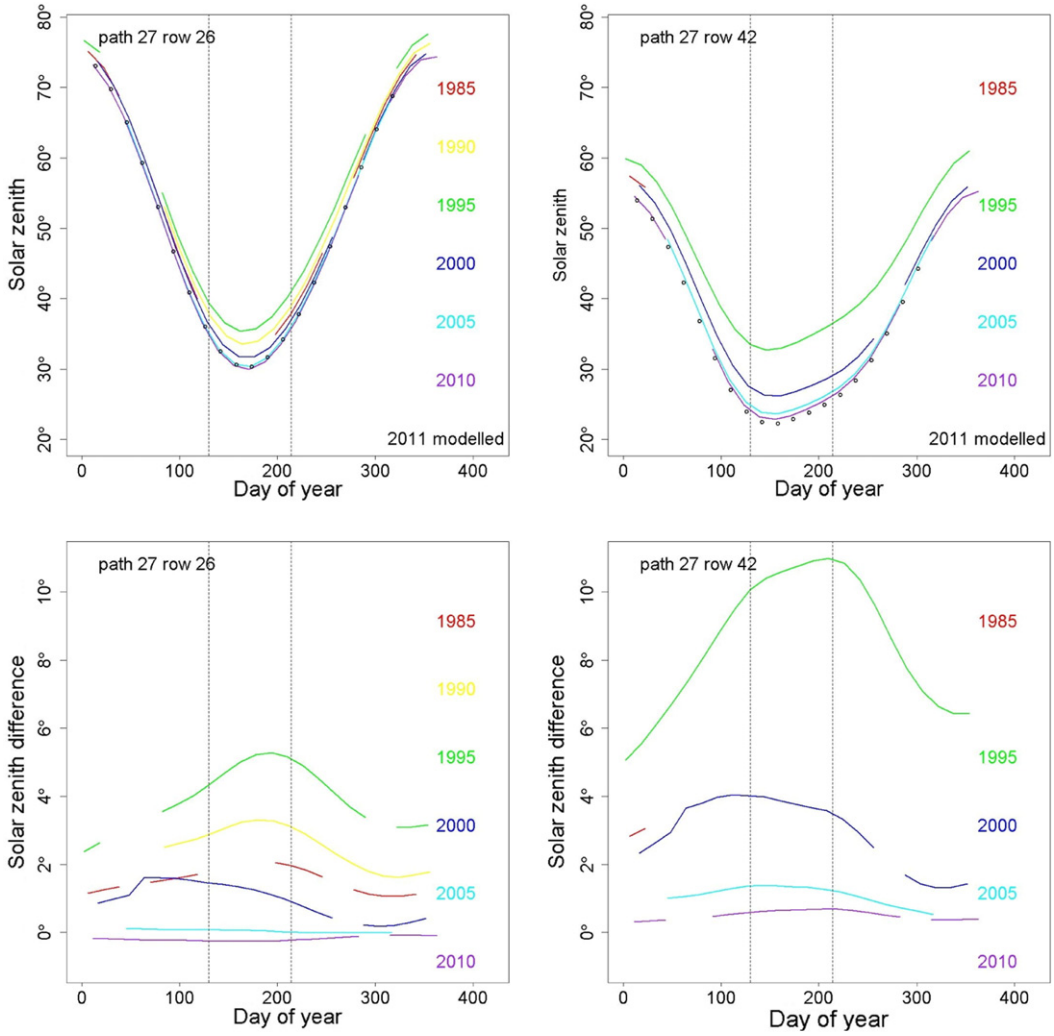

Fig. 2. Landsat 5 TM observed solar zenith angle ($\theta_{observed}$) (top) and solar zenith angle difference ($\theta_{observed} - \theta_{reference}$) (bottom) plotted as a function of the acquisition day of the year for Minnesota (path/row 27/26, left) and Texas (path/row 27/42, right). The colors show different acquisition years spaced five years apart from 1985 to 2010. The black dots shows the $\theta_{reference}$ plotted every 16 days for the 2011 Landsat acquisitions dates. The vertical lines show the days of the year six weeks before and six weeks after the June 21 summer solstice. Note, there were no available 1990 Landsat 5 TM data over the Texas site (Fig. 1).

4.3. Landsat 5 TM reflectance and NDVI time series modelling

4.3.1. Mean MODIS BRDF model parameters

The 12 month mean CONUS and CONUS land cover class specific BRDF spectral model parameter values are summarized for the red and NIR bands in Table 1. The f_{vol} and f_{geo} parameters weight the volumetric scattering and geometric-optical BRDF kernels respectively and have no direct physical meaning, although they can be conceptualized as describing the directional reflectance effects of inter-leaf and inter-crown canopy gaps respectively (Lucht et al., 2000). The f_{iso} parameter provides an additive reflectance term that reflects nadir viewing and solar geometry, and so can be considered as average BRDF-independent (i.e., isotropic) reflectance value (Roy et al., 2016b).

Fig. 4 illustrates the use of the different BRDF spectral model parameter and the impact of solar zenith changes on the modelled NBAR NDVI. The predicted NBAR NDVI derived for each fixed set of land cover specific (colored lines) and for the CONUS (black line) BRDF spectral model parameters for solar zenith angles from 20° to 80° are shown. This range of solar zenith angles is illustrated because the minimum solar zenith angle at the time of Landsat overpass is >20° for non-Antarctic acquisitions and although at high latitudes the Landsat solar zenith can be >80° (Bindschadler et al., 2008, Zhang et al., 2016), the MODIS BRDF retrieval and atmospheric correction techniques are unreliable at such high solar zenith angles (Schaaf et al., 2002; Lee and Kaufman, 1986).

Fig. 4 illustrates that the modelled NBAR NDVI increases with solar zenith angle, particularly above about 60°, and that the increases are different among the land cover classes. This NDVI dependency on solar zenith has been observed and modelled by other researchers as described in the Introduction. The most pronounced solar zenith sensitivity is for the structurally dominated (geometric-optically governed) land cover types, particularly the closed shrubland and the evergreen needleleaf forest classes, which has been observed and investigated previously (Gao et al., 2003). The barren or sparsely vegetated class has the least NDVI NBAR sensitivity to solar zenith, which is perhaps due to the low NDVI amplitude and not particularly due to low reflectance anisotropy (Huete, 1987; Deering et al., 1990). The CONUS mean NBAR NDVI values exhibit average solar zenith sensitivity. These results indicate that a change in the solar zenith due to orbit drift may cause significant NBAR NDVI changes, particularly at latitudes and times of the year when the solar zenith is high at the nominal Landsat overpass time. This is investigated in the following section, considering NBAR derived for the 12 month mean CONUS and the closed shrubland BRDF spectral model parameters as surrogates for average and particularly anisotropic surfaces respectively.

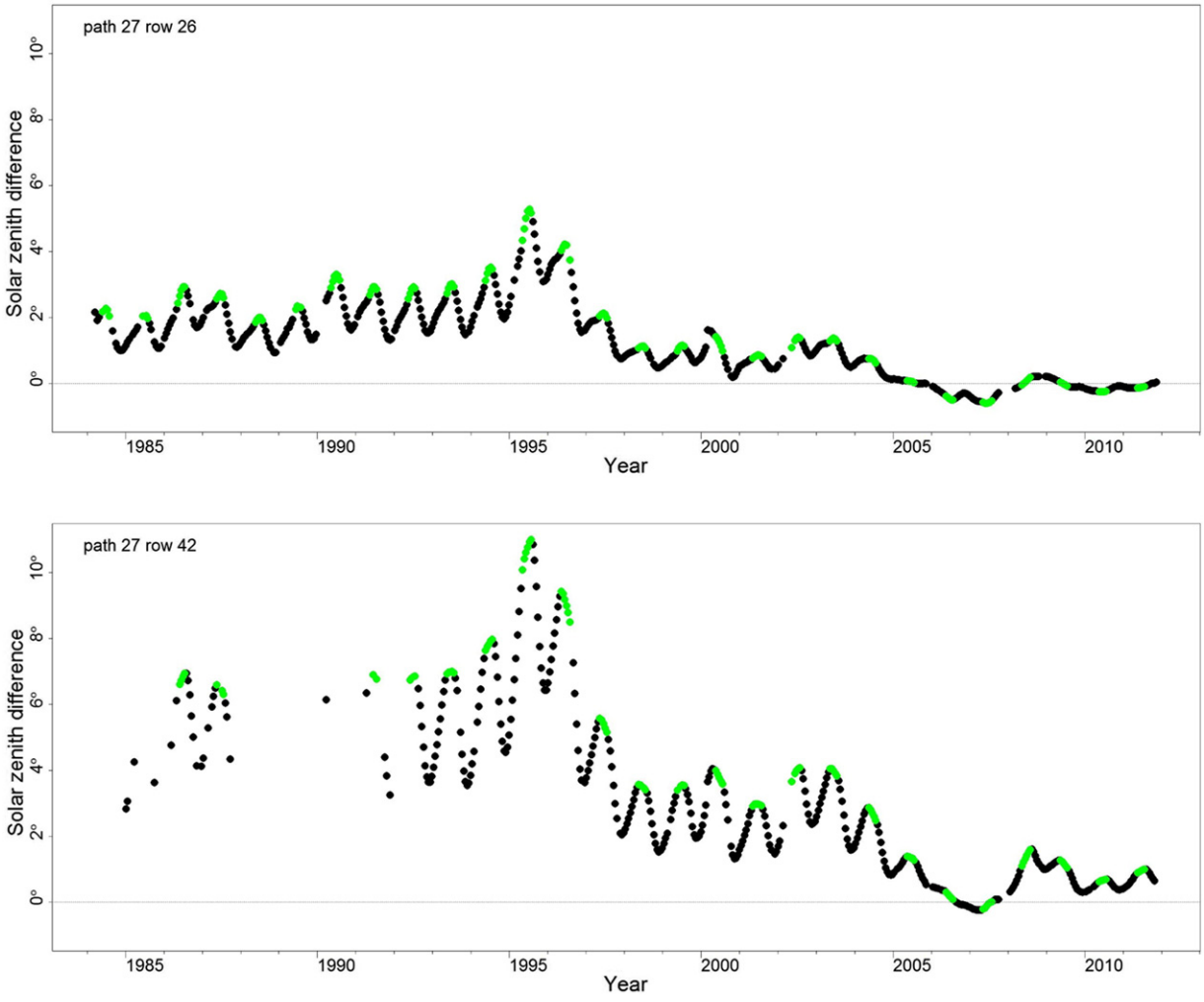

Fig. 3. 27 years of Landsat 5 TM solar zenith differences ($\theta_{observed} - \theta_{reference}$) plotted as a function of acquisition date for Minnesota (path/row 27/26, top) and Texas (path/row 27/42, bottom). The green colors show the summer (June 21 ± six weeks) difference values.

4.3.2. Modelled Landsat 5 TM reflectance and NDVI

Figs. 5 and 6 show the modelled $\rho_{red\ observed}$, $\rho_{NIR\ observed}$, and $NDVI_{observed}$ NBAR values derived using the 12 month mean CONUS (blue) and closed shrubland class (red) spectral BRDF model parameters for the 27 years of Minnesota and Texas Landsat 5 TM acquisitions. The NBAR variations evident in these figures are driven by $\theta_{observed}$ temporal changes only, no phenological, snow cover, or land cover changes are modelled (the BRDF spectral model parameters are

Table 1
Red and NIR CONUS and land cover specific BRDF spectral model parameter values, *n* is the number of 500 m highest quality and snow-free MODIS BRDF spectral parameters pixel values considered and varies spectrally because of the number of high-quality parameters in the MODIS BRDF/Albedo quality product (MCD43A2) varies spectrally.

Class	Red				NIR			
	n	f_{iso}	f_{vol}	f_{geo}	n	f_{iso}	f_{vol}	f_{geo}
Evergreen needleleaf forest	73,420,769	0.0546	0.0260	0.0159	72,945,739	0.2369	0.1775	0.0431
Evergreen broadleaf forest	3,140,442	0.0467	0.0278	0.0106	3,132,896	0.2663	0.1909	0.0292
Deciduous needleleaf forest	510,881	0.0571	0.0287	0.0114	495,839	0.2074	0.1405	0.0291
Deciduous broadleaf forest	65,759,474	0.0592	0.0296	0.0134	65,458,441	0.3241	0.1708	0.0508
Mixed forest	164,334,382	0.0493	0.0292	0.0114	163,281,787	0.2767	0.1695	0.0410
Closed shrublands	4,330,303	0.0875	0.0327	0.0258	4,317,408	0.2222	0.1654	0.0381
Open shrublands	166,861,668	0.2110	0.0624	0.0492	166,439,481	0.3052	0.1531	0.0518
Woody savannas	86,114,510	0.0751	0.0281	0.0185	85,815,927	0.2780	0.1803	0.0378
Savannas	6,309,508	0.0917	0.0436	0.0212	6,289,387	0.2579	0.1890	0.0320
Grasslands	336,410,414	0.1469	0.0656	0.0322	335,348,665	0.2704	0.2059	0.0296
Croplands	185,851,048	0.1140	0.0505	0.0217	184,466,616	0.3182	0.2083	0.0274
Urban and built-up	16,384,025	0.1149	0.0357	0.0248	16,305,600	0.2772	0.1623	0.0377
Cropland and natural vegetation mosaic	145,990,196	0.0812	0.0335	0.0173	145,170,752	0.3262	0.1931	0.0379
Barren or sparsely vegetated	18,160,663	0.3151	0.0918	0.0439	17,949,742	0.3784	0.1411	0.0416
CONUS mean	1,273,578,283	0.1131	0.0462	0.0247	1,267,418,280	0.2869	0.1833	0.0367

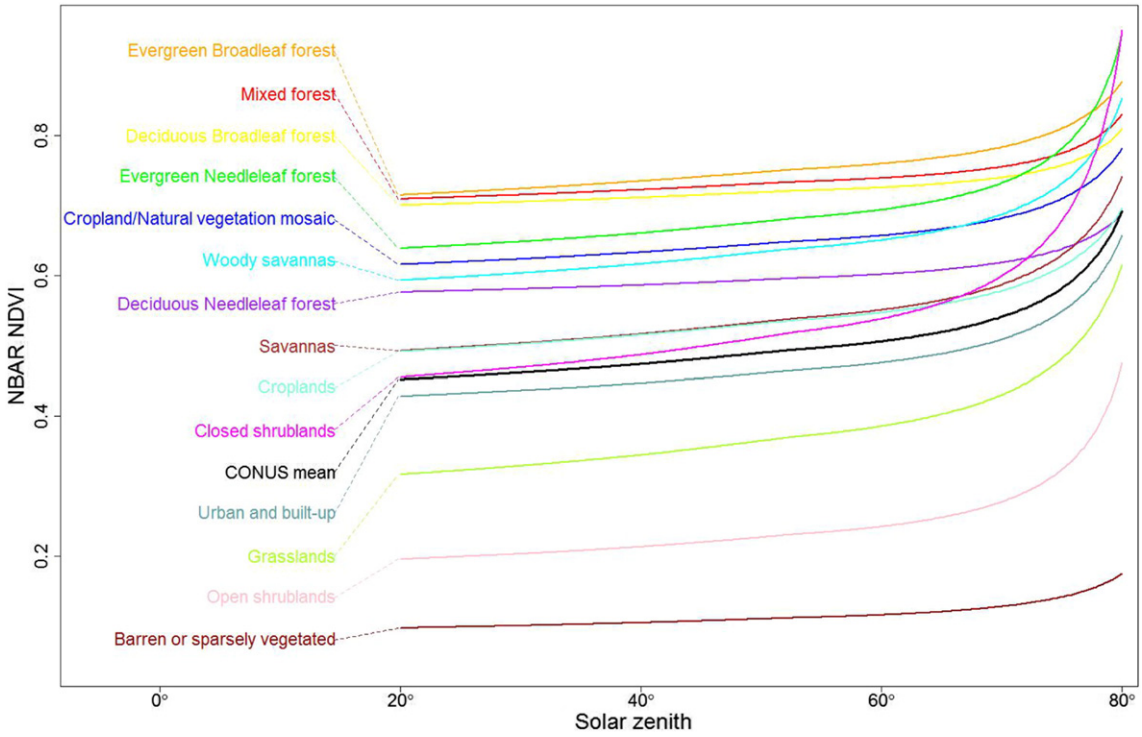

Fig. 4. Modelled NBAR NDVI plotted as a function of solar zenith; derived from red and NIR NBAR values computed as Eq. (1) setting the view zenith to 0°, solar zenith angles from 20° to 80°, and using fixed 12 month mean CONUS (black line) and 12 month mean CONUS land cover specific (colored lines) spectral BRDF model parameters. The legends are shown ordered from top to bottom in descending order of NBAR NDVI value at 20° solar zenith.

fixed). For both sites, the CONUS mean NBAR NDVI values are smaller than the closed shrubland equivalent values as observed in Fig. 4.

A seasonal NBAR variation is very evident, a similar modelled seasonal NBAR variation was found by Gao et al. (2014). Each year the maximum and minimum modelled NBAR $NDVI_{observed}$ values occur in the northern hemisphere winter and summer respectively. This is because the solar zenith angles at the time of Landsat overpass are maximal and minimal in the winter and summer respectively (Fig. 2) and NBAR NDVI increases with solar zenith (Fig. 4). The 27 year maximum modelled NBAR $NDVI_{observed}$ values occurred when the $\theta_{observed}$ was maximal, specifically, for the Minnesota and Texas Landsat 5 TM acquisitions sensed on December 20, 1995 ($\theta_{observed} = 77.5731°$) and January 5, 1996 ($\theta_{observed} = 61.3363°$) respectively. Over the 27 years the intra-annual (i.e., seasonal) range of the modelled NBAR $NDVI_{observed}$ values for the CONUS BRDF parameters (Figs. 5 and 6 bottom, blue) is about 0.1 (Minnesota) and 0.05 (Texas) and for the CONUS closed shrubland BRDF parameters (Figs. 5 and 6 bottom, red) is nearly twice as large. This annual variation may have implications for Landsat NDVI based phenological studies where solar zenith effects are assumed to be negligible (Fisher and Mustard, 2007; Kovalskyy et al., 2012; Bhandari et al., 2012; Melaas et al., 2013).

4.3.3. Evaluation of modelled Landsat 5 TM reflectance and NDVI variation

The modelled reflectance changes due to Landsat 5 TM orbit changes are apparent in Figs. 5 and 6 but are largely obscured by seasonal $\theta_{observed}$ driven NBAR variations. Comparison of the modelled NBAR values derived with solar zenith set to $\theta_{observed}$ and set to $\theta_{reference}$ reduces the seasonal solar zenith variation (Fig. 2) and reveals the change in modelled reflectance due to Landsat 5 TM orbit changes relative to year 2011. This comparison is illustrated in Figs. 7 and 8 for Minnesota and Texas respectively. These figures show the 27 years of modelled red, NIR and NBAR differences ($\Delta^{red} = \rho_{red\ observed} - \rho_{red\ reference}$, $\Delta^{NIR} = \rho_{NIR\ observed} - \rho_{NIR\ reference}$, $\Delta^{NDVI} = NDVI_{observed} - NDVI_{reference}$) generated using the closed shrubland class spectral BRDF model parameters. Tables 2 and 3 summarize the 27 year Δ^{NDVI} NBAR variation illustrated in Figs. 7 and 8 and also for the results generated using the land cover specific BRDF parameters. The mean absolute Δ^{NDVI} NBAR differences over the 27 years are very small, typically only several thousandths of an NDVI unit, and no greater than 0.0072 (Minnesota) and 0.0060 (Texas) for the closed shrubland class. The mean values do not capture the temporal trends in the differences which are investigated below.

The straight lines in Figs. 7 and 8 show the OLS regression fits of the Δ^{NDVI} NBAR values as a function of the date of acquisition and so capture the first-order 27 year reflectance trends introduced by the orbit drift. The NBAR Δ^{red} and Δ^{NIR} values have an increasing trend (top and middle of Figs. 7 and 8) and the NBAR Δ^{NDVI} values have a decreasing trend (bottom of Figs. 7 and 8) as the solar zenith and NDVI are positively correlated (Fig. 4). The regressions fits are all significant although the r^2 values are not high (<0.6 Minnesota and <0.7 Texas) due to the influence of periodic station keeping maneuvers that are most apparent in the NBAR Δ^{NDVI} results (bottom rows of Figs. 7 and 8).

Long term analyses of Landsat greening trends often consider only peak-vegetation conditions (McManus et al., 2012, Fraser et al., 2012; Ju and Masek, 2016), and therefore the OLS regressions considering only the northern hemisphere summer acquisitions are also examined. The modelled Minnesota NBAR Δ^{NDVI} OLS regression slopes (Fig. 7. bottom) and their goodness of fit (Table 2) are quite different when considering only the summer data (r^2 ~0.5) compared to considering all the data (r^2 ~0.2). This is because the Minnesota winter solar zenith angles are high, often >60° (Fig. 2) and under these conditions the NBAR NDVI increases particularly rapidly with respect to solar zenith (Fig. 4) and so even small differences between $\theta_{observed}$ and $\theta_{reference}$ may cause large NBAR Δ^{NDVI} values. Conversely, the Texas OLS regressions lines considering all the data and only the summer data (Fig. 8, Table 3) are similar because the Texas winter solar zenith angles are lower and <60° (Fig. 2). The slopes of the illustrated modelled NBAR Δ^{NDVI} regression lines for Minnesota are 0.0005 NDVI/year (all data) and 0.0002 NDVI/year (summer data), and for Texas are 0.0006 NDVI/year. The equivalent slopes for

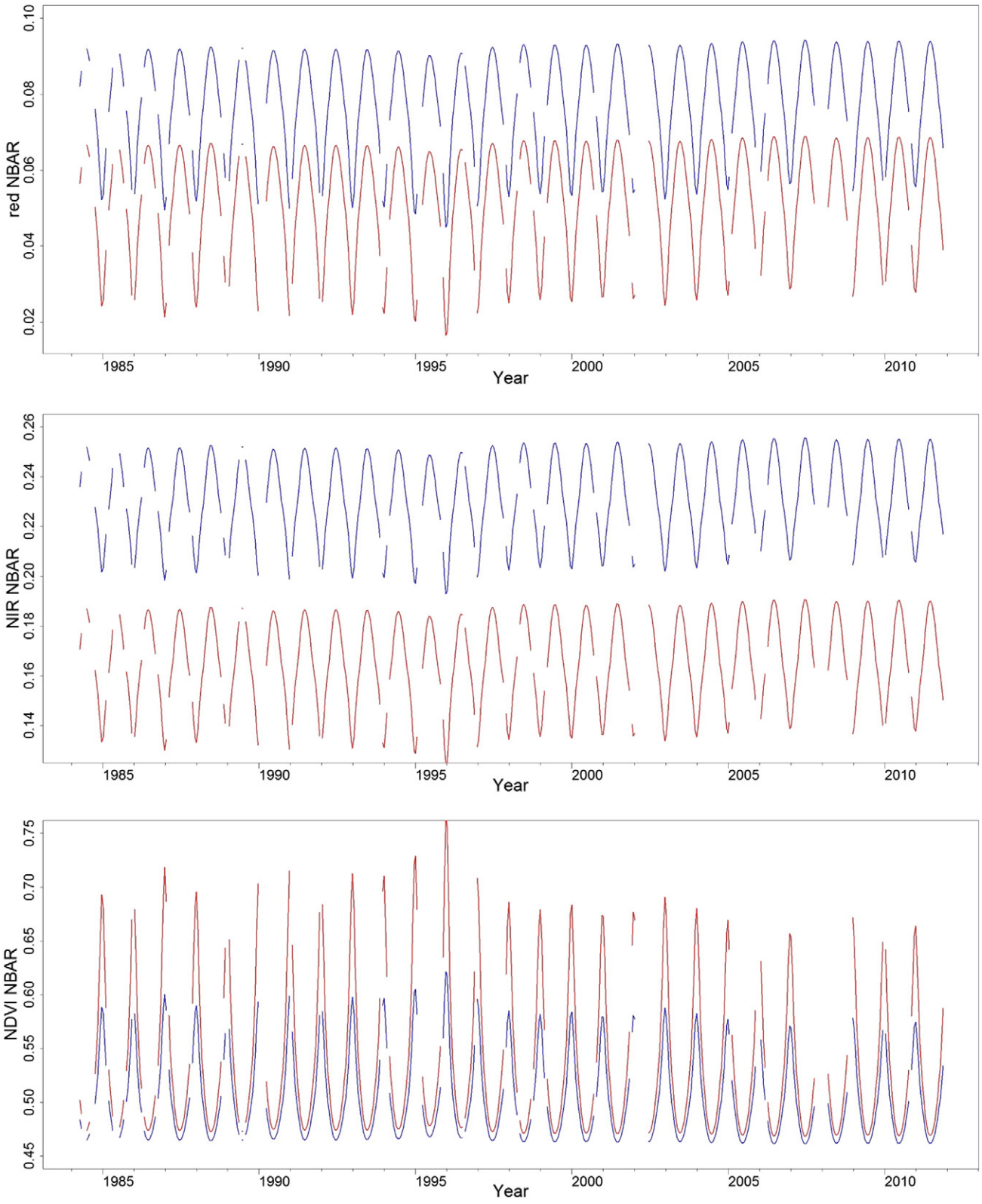

Fig. 5. 27 years of Landsat 5 TM Minnesota (path/row 27/26) modelled NBAR red ($\rho_{red\ observed}$), NIR ($\rho_{NIR\ observed}$) and NDVI ($NDVI_{observed}$) values computed using the fixed 12 month mean CONUS (blue) and closed shrubland class (red) spectral BRDF model parameters and setting the view zenith to 0° and the solar zenith to $\theta_{observed}$.

the CONUS and the land cover specific BRDF spectral models are smaller (Tables 2 and 3). The slope magnitudes are small, for example, for Texas they imply that the modelled NDVI at Landsat 5 launch was about 0.016 greater than in 2011. Clearly, different trends will be obtained by considering periods of stable overpass times (e.g., from approximately 1984 to 1994, or from 2007 to 2011) and periods of rapidly changing overpass times (e.g., from approximately 1995 to 2000, or from 2003 to 2007) (Fig. 1).

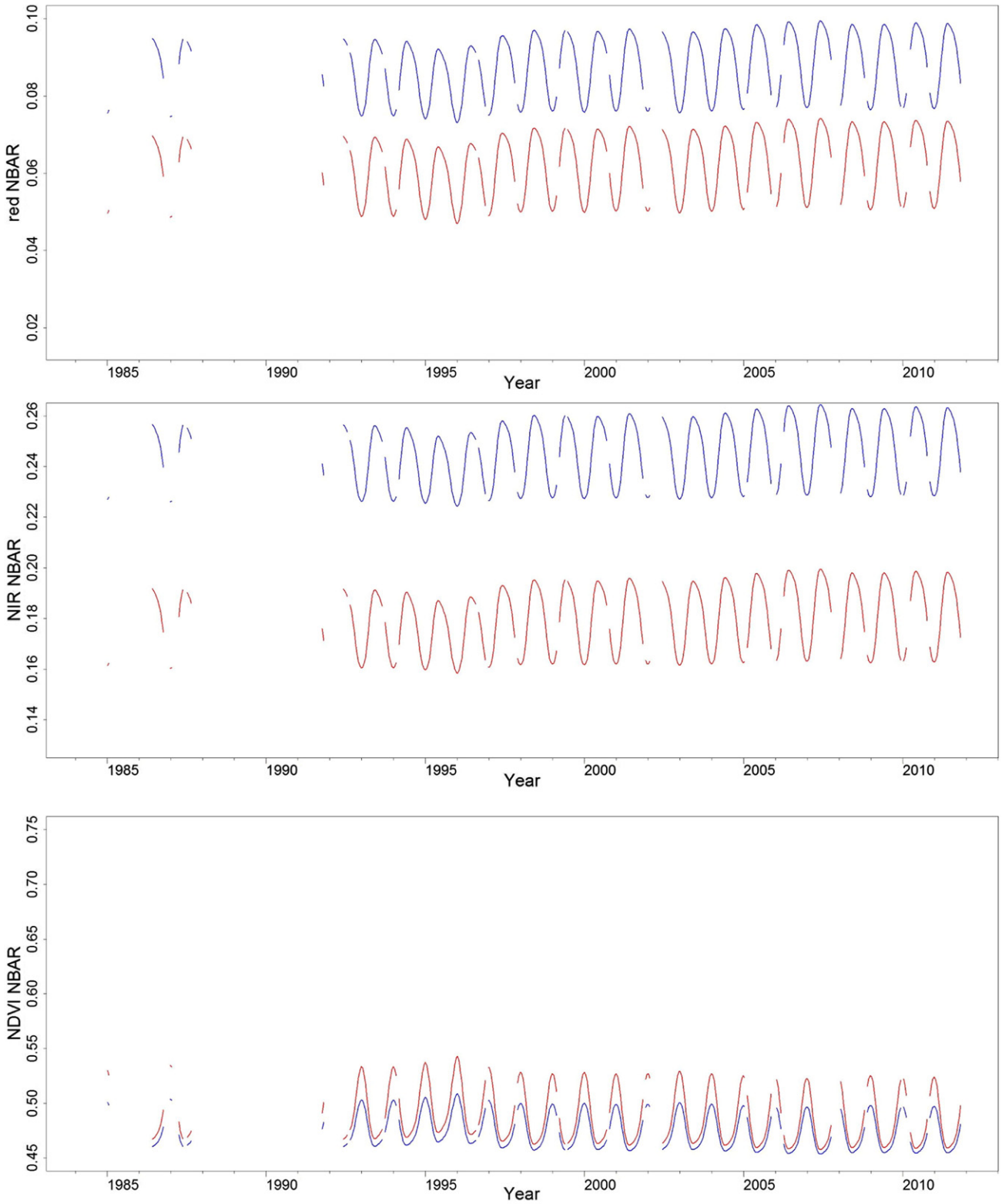

Fig. 6. 27 years of Landsat 5 TM Texas (path/row 27/42) modelled NBAR red ($\rho_{red\ observed}$), NIR ($\rho_{NIR\ observed}$) and NDVI ($NDVI_{observed}$) values computed using the fixed 12 month mean CONUS (blue) and closed shrubland class (red) spectral BRDF model parameters and setting the view zenith to 0° and the solar zenith to $\theta_{observed}$.

Figs. 7 and 8 (and Tables 2 and 3) illustrate that temporal comparison of Landsat 5 data acquired on approximately the same (i.e., anniversary) dates from certain different years will result in large reflectance and NDVI differences due only to orbit changes. In particular, the maximum and minimum modelled NBAR Δ^{NDVI} values occurred, for any of the BRDF parameters, in 1995 and 2007 respectively and correspond to the early t_{local} values in 1995 and when t_{local} and $t_{reference}$ were most similar in 2007 (Fig. 1). The smallest of the tabulated modelled NBAR Δ^{NDVI} ranges were 0.0161 (Minnesota) and 0.0045 (Texas) for the barren or sparsely vegetated class (which has the lowest NBAR NDVI

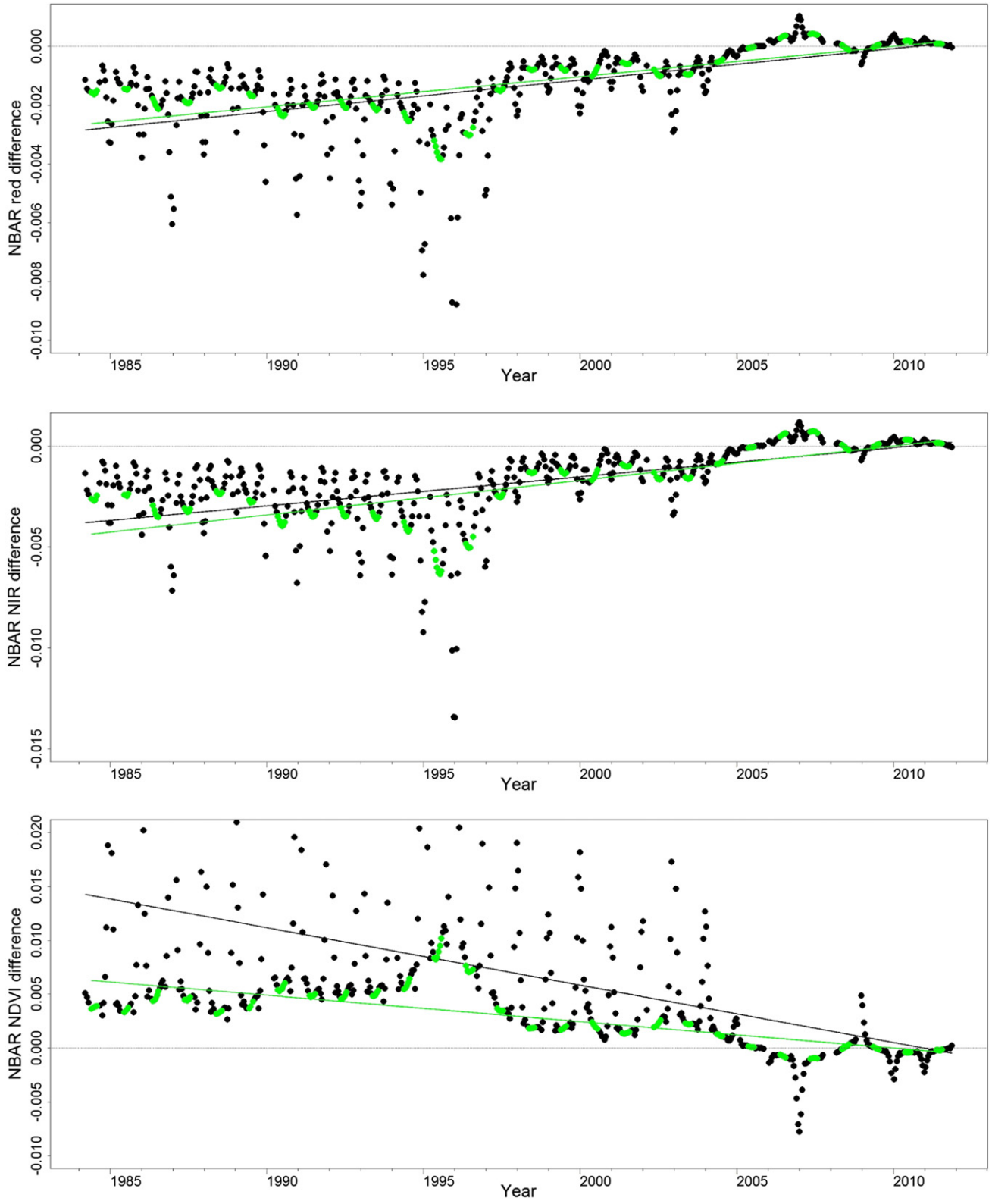

Fig. 7. 27 years of modelled Landsat 5 TM Minnesota (path/row 27/26) NBAR difference values for $\Delta^{red} = \rho_{red\ observed} - \rho_{red\ reference}$, $\Delta^{NIR} = \rho_{NIR\ observed} - \rho_{NIR\ reference}$, and $\Delta^{NDVI} = NDVI_{observed} - NDVI_{reference}$ computed using the fixed 12 month mean closed shrubland class spectral BRDF model parameters and setting the view zenith to 0° and the solar zenith to $\theta_{observed}$ and $\theta_{reference}$. The black lines show the OLS regression lines of these data. The green colors show the summer (June 21 ± six weeks) NBAR difference values and their regression lines.

modelled sensitivity to solar zenith (Fig. 4)). The CONUS BRDF parameters had intermediate modelled NBAR Δ^{NDVI} ranges of 0.0505 and 0.0132 for Minnesota and Texas respectively. As expected, the greatest modelled NBAR Δ^{NDVI} ranges were for the closed shrubland class and were 0.1085 (Minnesota) and 0.0208 (Texas). The magnitude of these differences is not insignificant and is discussed in Section 5.

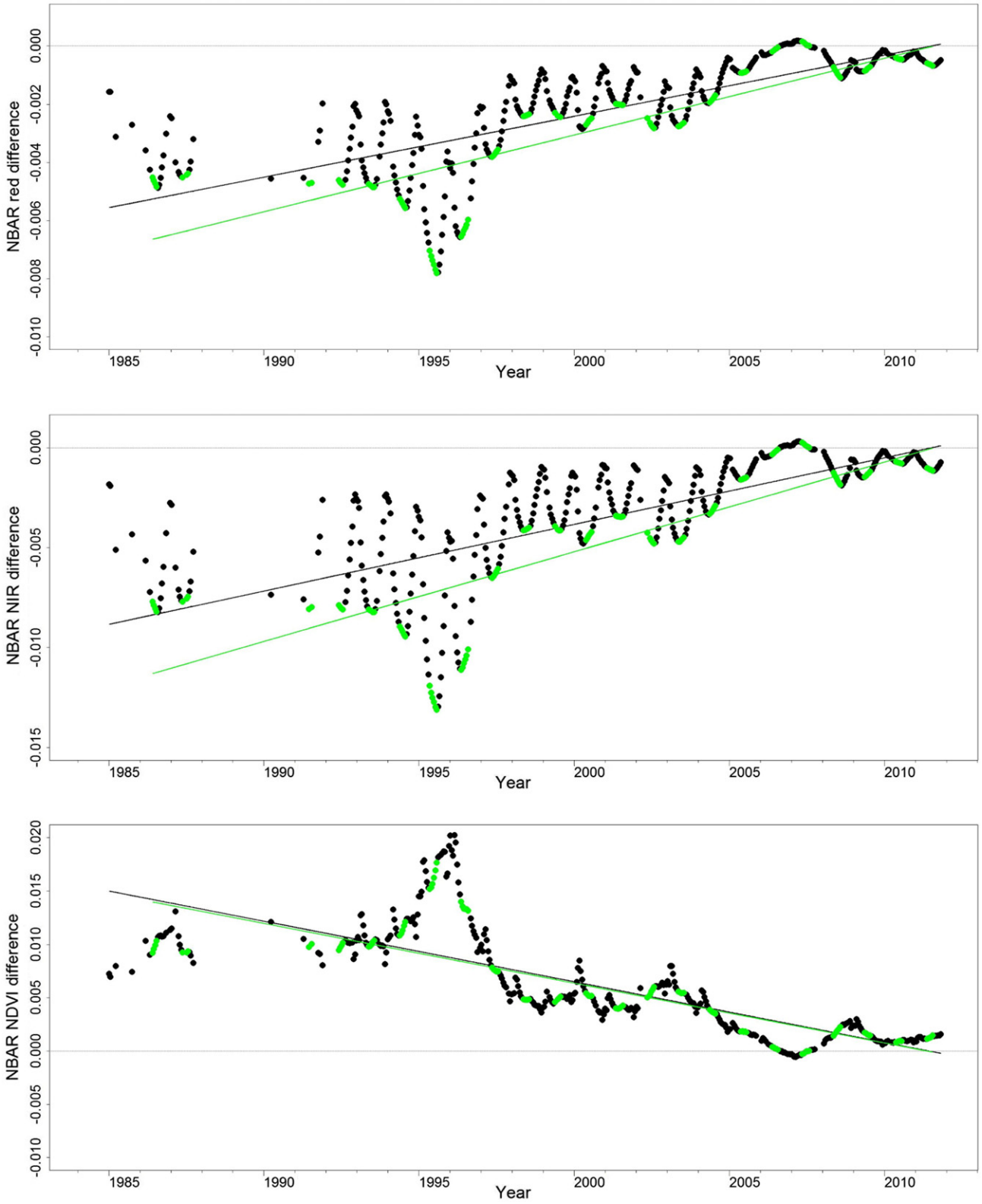

Fig. 8. 27 years of modelled Landsat 5 TM Texas (path/row 27/42) NBAR difference values for $\Delta^{red} = \rho_{red\ observed} - \rho_{red\ reference}$, $\Delta^{NIR} = \rho_{NIR\ observed} - \rho_{NIR\ reference}$, and $\Delta^{NDVI} = NDVI_{observed} - NDVI_{reference}$ computed using the fixed 12 month mean closed shrubland class spectral BRDF model parameters and setting the view zenith to 0° and the solar zenith to $\theta_{observed}$ and $\theta_{reference}$. The black lines show the OLS regression lines of these data. The green colors show the summer (June 21 ± six weeks) NBAR difference values and their regression lines.

4.4. Example Landsat 5 TM images

Fig. 9 shows the NIR reflectance, NDVI, and solar zenith extracted from twelve Landsat 5 TM images. The values for three documented sites (Vogelmann et al., 2016) selected over areas of coniferous forest with only gradual Landsat NDVI increase (green) and decrease (orange), and an unchanging pumice desert with dispersed small herbaceous plants (blue) are illustrated. Pixel values for nine adjacent

Table 2
Summary statistics of the 27 years of modelled Minnesota (path/row 27/26) NDVI NBAR differences ($\Delta^{NDVI} = NDVI_{observed} - NDVI_{reference}$) and OLS regression parameters derived considering different 12 month mean BRDF spectral parameters. The 27 year range of Δ^{NDVI} values and the mean absolute (Δ^{NDVI}) over the 27 years are defined with NDVI units; the occurrence of the maximum (Δ^{NDVI}) and minimum (Δ^{NDVI}) values are shown as decimal years. The results are tabulated with a row order ranked by decreasing Range (Δ^{NDVI}). The values in parentheses are for the summer months (June 21 ± six weeks) only. All of the regressions were significant with p-values <0.0001.

12 month mean BRDF spectral parameter source	Range (Δ) = Max. (Δ) – Min. (Δ)	Mean/Δ/	Date of maximum (Δ)	Date of minimum (Δ)	OLS coefficients m and c where regression is $\Delta = m$ date $+ c$	OLS regression r^2
Closed shrublands	0.1085	0.0072	1995.967	2007.005	$\Delta = -0.0005$ date $+ 1.0710$	0.1337
	(0.0112)	(0.0030)	(1995.573)	(2007.356)	($\Delta = -0.0002$ date $+ 0.4929$)	(0.5563)
Evergreen needleleaf forest	0.0667	0.0046	1995.967	2007.005	$\Delta = -0.0003$ date $+ 0.6804$	0.1416
	(0.0074)	(0.0020)	(1995.573)	(2007.356)	($\Delta = -0.0002$ date $+ 0.3336$)	(0.5572)
Grasslands	0.0623	0.0050	1995.967	2007.005	$\Delta = -0.0004$ date $+ 0.7561$	0.1794
	(0.0095)	(0.0026)	(1995.573)	(2007.356)	($\Delta = -0.0002$ date $+ 0.4269$)	(0.5611)
Open shrublands	0.0619	0.0041	1995.967	2007.005	$\Delta = -0.0003$ date $+ 0.6130$	0.1324
	(0.0062)	(0.0017)	(1995.573)	(2007.356)	($\Delta = -0.0001$ date $+ 0.2734$)	(0.5567)
Woody savannas	0.0550	0.0043	1995.967	2007.005	$\Delta = -0.0003$ date $+ 0.6409$	0.1712
	(0.0079)	(0.0022)	(1995.573)	(2007.400)	($\Delta = -0.0002$ date $+ 0.3597$)	(0.5604)
Savannas	0.0517	0.0042	1995.967	2007.005	$\Delta = -0.0003$ date $+ 0.6282$	0.1817
	(0.0081)	(0.0022)	(1995.573)	(2007.356)	($\Delta = -0.0002$ date $+ 0.3654$)	(0.5611)
All CONUS	0.0505	0.0040	1995.967	2007.005	$\Delta = -0.0003$ date $+ 0.5980$	0.1746
	(0.0075)	(0.0021)	(1995.573)	(2007.356)	($\Delta = -0.0002$ date $+ 0.3377$)	(0.5606)
Urban and built-up	0.0493	0.0037	1995.967	2007.005	$\Delta = -0.0003$ date $+ 0.5604$	0.1614
	(0.0065)	(0.0018)	(1995.573)	(2007.356)	($\Delta = -0.0001$ date $+ 0.2874$)	(0.5582)
Croplands	0.0404	0.0036	1995.967	2007.005	$\Delta = -0.0003$ date $+ 0.5480$	0.2140
	(0.0079)	(0.0022)	(1995.573)	(2007.356)	($\Delta = -0.0002$ date $+ 0.3629$)	(0.5643)
Cropland/Natural Vegetation mosaic	0.0339	0.0028	1995.967	2007.005	$\Delta = -0.0002$ date $+ 0.4291$	0.1941
	(0.0058)	(0.0016)	(1995.573)	(2007.575)	($\Delta = -0.0001$ date $+ 0.2656$)	(0.5635)
Evergreen broadleaf forest	0.0319	0.0028	1995.967	2007.005	$\Delta = -0.0002$ date $+ 0.4295$	0.2166
	(0.0065)	(0.0018)	(1995.573)	(2007.356)	($\Delta = -0.0001$ date $+ 0.2989$)	(0.5650)
Mixed forest	0.0247	0.0020	1995.967	2007.005	$\Delta = -0.0002$ date $+ 0.3032$	0.1912
	(0.0044)	(0.0012)	(1995.573)	(2007.400)	($\Delta = -0.0001$ date $+ 0.1995$)	(0.5628)
Deciduous needleleaf forest	0.0237	0.0019	1995.967	2007.005	$\Delta = -0.0001$ date $+ 0.2845$	0.1749
	(0.0035)	(0.0009)	(1995.573)	(2007.400)	($\Delta = -0.0001$ date $+ 0.1548$)	(0.5565)
Deciduous broadleaf forest	0.0227	0.0018	1995.967	2007.005	$\Delta = -0.0001$ date $+ 0.2670$	0.1794
	(0.0037)	(0.0010)	(1995.573)	(2007.400)	($\Delta = -0.0001$ date $+ 0.1684$)	(0.5654)
Barren or sparsely vegetated	0.0161	0.0013	1995.967	2007.005	$\Delta = -0.0001$ date $+ 0.2017$	0.1854
	(0.0026)	(0.0007)	(1995.573)	(2007.356)	($\Delta = -0.0001$ date $+ 0.1163$)	(0.5613)

Table 3
Summary statistics of the 27 years of modelled Texas (path/row 27/42) NDVI NBAR difference ($\Delta^{NDVI} = NDVI_{observed} - NDVI_{reference}$) and the OLS regression parameters derived considering different 12 month mean BRDF spectral parameters. All of the regressions were significant with p-values <0.0001.

12 month mean BRDF spectral parameter source	Range (Δ) = Max. (Δ) − Min. (Δ)	Mean/Δ/	Date of maximum (Δ)	Date of minimum (Δ)	OLS coefficients m and c where regression is $\Delta = m$ date $+ c$	OLS regression r^2
Closed shrublands	0.0208	0.0060	1996.142	2007.137	$\Delta = -0.0006$ date $+ 1.1421$	0.6160
	(0.0179)	(0.0059)	(1995.573)	(2007.356)	($\Delta = -0.0006$ date $+ 1.1256$)	(0.6678)
Grasslands	0.0168	0.0051	1996.142	2007.137	$\Delta = -0.0005$ date $+ 0.9642$	0.6239
	(0.0157)	(0.0052)	(1995.573)	(2007.356)	($\Delta = -0.0005$ date $+ 0.9945$)	(0.6715)
Savannas	0.0141	0.0043	1996.142	2007.137	$\Delta = -0.0004$ date $+ 0.8193$	0.6243
	(0.0134)	(0.0045)	(1995.573)	(2007.356)	($\Delta = -0.0004$ date $+ 0.8573$)	(0.6716)
Woody savannas	0.0140	0.0043	1996.142	2007.137	$\Delta = -0.0004$ date $+ 0.8075$	0.6239
	(0.0132)	(0.0044)	(1995.573)	(2007.356)	($\Delta = -0.0004$ date $+ 0.8407$)	(0.6713)
Croplands	0.0138	0.0042	1995.616	2007.181	$\Delta = -0.0004$ date $+ 0.7951$	0.6235
	(0.0135)	(0.0046)	(1995.573)	(2007.356)	($\Delta = -0.0004$ date $+ 0.8681$)	(0.6754)
Evergreen needleleaf forest	0.0136	0.0040	1996.142	2007.093	$\Delta = -0.0004$ date $+ 0.7626$	0.6197
	(0.0122)	(0.0040)	(1995.573)	(2007.356)	($\Delta = -0.0004$ date $+ 0.7658$)	(0.6689)
All CONUS	0.0132	0.0040	1996.142	2007.093	$\Delta = -0.0004$ date $+ 0.7593$	0.6243
	(0.0124)	(0.0041)	(1995.573)	(2007.356)	($\Delta = -0.0004$ date $+ 0.7905$)	(0.6718)
Open shrublands	0.0120	0.0034	1996.011	2007.093	$\Delta = -0.0003$ date $+ 0.6396$	0.6136
	(0.0100)	(0.0033)	(1995.573)	(2007.356)	($\Delta = -0.0003$ date $+ 0.6253$)	(0.6672)
Urban and built-up	0.0118	0.0035	1996.011	2007.093	$\Delta = -0.0003$ date $+ 0.6612$	0.6201
	(0.0105)	(0.0035)	(1995.573)	(2007.356)	($\Delta = -0.0003$ date $+ 0.6646$)	(0.6703)
Evergreen broadleaf forest	0.0114	0.0034	1995.616	2007.137	$\Delta = -0.0003$ date $+ 0.6449$	0.6183
	(0.0112)	(0.0038)	(1995.573)	(2007.356)	($\Delta = -0.0004$ date $+ 0.7191$)	(0.6759)
Cropland/Natural Vegetation mosaic	0.0101	0.0031	1995.616	2007.137	$\Delta = -0.0003$ date $+ 0.5870$	0.6246
	(0.0098)	(0.0033)	(1995.573)	(2007.356)	($\Delta = -0.0003$ date $+ 0.6304$)	(0.6744)
Mixed forest	0.0075	0.0023	1995.660	2007.181	$\Delta = -0.0002$ date $+ 0.4293$	0.6179
	(0.0074)	(0.0025)	(1995.573)	(2007.356)	($\Delta = -0.0002$ date $+ 0.4759$)	(0.6749)
Deciduous broadleaf forest	0.0065	0.0019	1995.616	2007.225	$\Delta = -0.0002$ date $+ 0.3642$	0.6200
	(0.0063)	(0.0021)	(1995.573)	(2007.400)	($\Delta = -0.0002$ date $+ 0.4010$)	(0.6731)
Deciduous needleleaf forest	0.0062	0.0019	1996.142	2007.181	$\Delta = -0.0002$ date $+ 0.3529$	0.6212
	(0.0057)	(0.0019)	(1995.573)	(2007.356)	($\Delta = -0.0002$ date $+ 0.3597$)	(0.6705)
Barren or sparsely vegetated	0.0045	0.0014	1996.142	2007.093	$\Delta = -0.0001$ date $+ 0.2622$	0.6253
	(0.0043)	(0.0014)	(1995.573)	(2007.356)	($\Delta = -0.0001$ date $+ 0.2750$)	(0.6729)

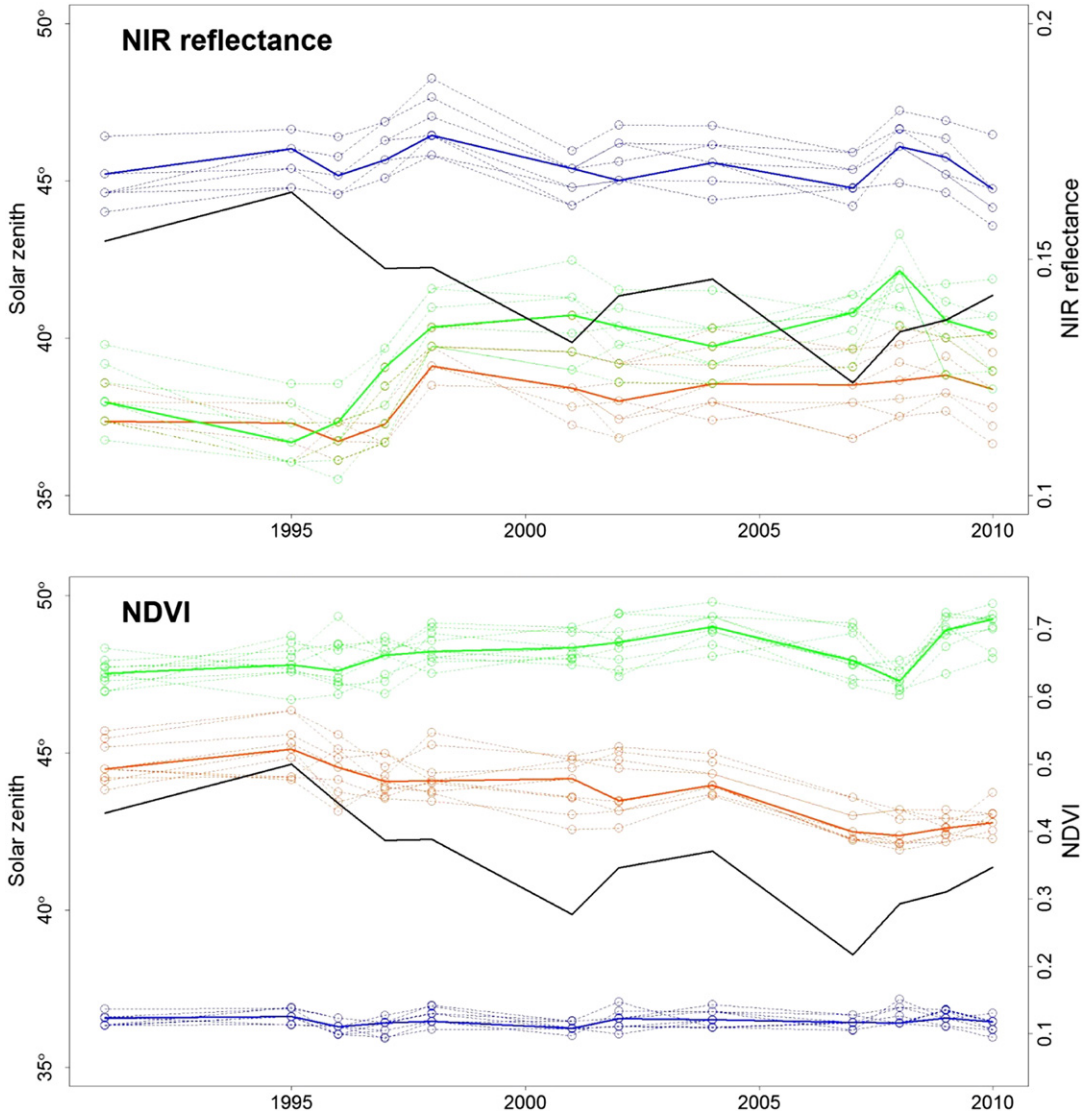

Fig. 9. Landsat 5 TM surface NIR reflectance and NDVI values for twelve summer anniversary date images sensed from 1991 to 2010 (open circles) and median values (solid colored lines) and the corresponding Landsat 5 TM solar zenith angles (solid black lines). Results shown for 3 × 3 30 m pixels located at three sites around Crater Lake National Park, Oregon, USA. The three sites are described in Vogelmann et al. (2016) and are for areas of coniferous forest with gradual NDVI increase (green), coniferous forest with gradual NDVI decrease (orange), and sparsely vegetated pumice desert (blue).

30 m pixels (colored circles) and the median values (colored solid lines) at each site are shown. The red surface reflectance values are not illustrated because the vegetated site red reflectance values are three times lower than the desert values making it hard to illustrate them on a single graph.

Due to the careful Landsat 5 image selection and processing (Section 2.5) the values in Fig. 9 should reflect only actual surface changes and the impacts of Landsat 5 solar zenith changes. Summer anniversary images acquired no more than ten days apart were used and so nominally the surface was sensed under similar solar conditions given a constant Landsat orbit. However, the images span the period with the greatest Landsat 5 TM satellite overpass time change. The illustrated maximum solar zenith (44.6332°) and minimum solar zenith (38.5769°) occurred for images sensed in 1995 and 2007 respectively which was also the years with maximum and minimum solar zenith observed in the Texas and Minnesota metadata time series (Fig. 1).

The Fig. 9 results show actual Landsat 5 TM data and provide support for the modelled based findings of this paper. The maximum and minimum NDVI values for the site with decreasing NDVI (orange), and the minimum and maximum and reflectance values for both vegetation sites, occurred in 1995 and around 2007 respectively which match the years of maximum and minimum solar zenith respectively. The Landsat 5 TM NIR and NDVI time series appear temporally correlated with the solar zenith angle. There are insufficient data to reliably de-trend the reflectance and NDVI values and so interpretation of correlations between these data and the solar zenith angles should be treated with caution. However, the median NDVI values have correlations with solar zenith of 0.81 for the decreasing vegetation (orange), −0.20 for the increasing vegetation (green), and 0.13 for the desert (blue) data. The small absolute correlation value for the increasing vegetation data is because the solar zenith is decreasing with year and so the correlation is reduced. The desert correlation is small (0.13) likely because the desert NDVI is less anisotropic, and certainly this is apparent for the BRDF modelled "barren or sparsely vegetated" class NDVI results shown in Fig. 4. The median vegetation NIR reflectance values have correlations with solar zenith of −0.66 and −0.87 for the orange and green data respectively and the red reflectance values have correlations of −0.82 and −0.45 for the orange and green data respectively. This negative correlation was also apparent in the BRDF modelled results whereby red and NIR NBAR reflectance decreased with increasing solar zenith (Figs. 5 and 6).

These results provide support for the modelled based findings of this paper. However, as noted earlier, even for anniversary date

observations, inter-annual variations in the surface state (e.g., between year soil moisture and vegetation condition variations) may be conflated with Landsat 5 TM orbit change induced reflectance effects. Further, as noted by Vogelmann et al. (2016), what exactly is happening at the sites over the Landsat 5 TM record is unknown.

5. Discussion and conclusion

In this paper irregular Landsat 5 station keeping maneuvers (orbit burns) are shown to have resulted in local overpass time changes much greater than ±15 min from the original specified 9:45 a.m. mean sunlit equatorial crossing time. Over the 27 years of Landsat 5 TM observations (March 1984 to November 2011) the range (maximum minus minimum) of the overpass times were 0.9153 and 0.9174 h for Landsat path/rows located in Minnesota (centered on 91.9363°W 48.8687°N) and Texas (centered on 98.9661°W 26.0011°N) respectively. These nearly 1 hour changes resulted in changes in the Landsat 5 observed solar zenith angle of >10°.

The observed solar zenith angles were compared with a reference year 2011 solar zenith considering a total of 567 (Minnesota) and 447 (Texas) acquisitions. The reference year 2011 solar zenith was derived using an astronomical model (Blanco-Muriel et al., 2001) parameterized with the Landsat acquisition center latitude, longitude, date of acquisition, and the modelled 2011 local overpass time at that latitude. The modelled 2011 local overpass time was defined as a function of the Landsat acquisition center latitude using a published statistical model (Zhang et al., 2016). Over the 27 years of Landsat 5 acquisitions the mean absolute solar zenith angles differences between the observed and the 2011 modelled solar zenith angles were 1.4° and 3.2°, and the maximum differences were 5.9° and 11.2°, for Minnesota and Texas respectively. The Texas mean absolute and maximum solar zenith angle differences of 3.2° and 11.2° are about half of the maximum 7.5° Landsat viewing zenith angle and are nearly comparable to the 15° Landsat field of view respectively. Thus, assuming the principal of reciprocity, whereby switching the solar and viewing geometry will provide similar directional reflectance (Kriebel, 1996; Snyder, 1998), the orbit induced solar zenith changes are expected to cause Landsat directional reflectance artifacts comparable to those associated with Landsat view zenith variations (Gao et al., 2014; Roy et al., 2016b).

Long term analyses of Landsat greening trends and responses of vegetation to climate and anthropogenic influences are expected to be increasingly undertaken to take advantage of the growing multi-sensor Landsat data record (Roy et al., 2014). Considerable effort has been expended on developing vegetation index time series fitting functions to detect trends and seasonal changes in satellite time series (Tucker et al., 2001; Jönsson and Eklundh, 2004; Verbesselt et al., 2010; Fensholt et al., 2012). In this study the change in reflectance due to Landsat 5 orbit changes relative to year 2011 were isolated by quantifying the difference between modelled NBAR derived independently for the Landsat 5 observed and the reference year 2011 solar zenith angles. The modelled NBAR values were derived using the MODIS Ross-Thick/Li-Sparse-Reciprocal BRDF model and fixed 12 month mean CONUS and land cover specific BRDF spectral model parameters. Ordinarly least squares (OLS) linear regression fits of the modelled NBAR difference values as a function of the acquisition date indicated an increasing trend in red and near-infrared NBAR and a decreasing trend in NDVI NBAR due to orbit changes. The OLS regressions fits were not high due to the influence of periodic station keeping maneuvers but were significant (p-values <0.0001). The trends may cause spurious detection of "browning" vegetation events and underestimation of greening trends over the (near climate length) 27 year data record. However, the magnitude of the trends were small, no more than 0.0006 NDVI/year, equivalent to about a 0.016 NDVI change over the Landsat 5 TM data record.

The most important finding of this study is that comparison of certain years of Landsat 5 data may result in significant reflectance and NDVI differences due only to Landsat 5 orbit changes. The greatest differences will occur when 1995 Landsat 5 TM data are compared with 2007 to 2011 data as in these periods the Landsat 5 local overpass times were nearly 1 h different. The reported analysis found that NDVI values could be up to 0.1085 greater in 1995 than in 2011 for anisotropic land cover types and up to 0.0505 greater for average CONUS land cover types. This difference in magnitude is not insignificant and is comparable or greater than other non-surface perturbations. For example, the mean atmospheric correction residual error for Landsat NDVI was found to be 3.1% and 6.3% using state of the practice radiative transfer based atmospheric correction methods (Ju et al., 2012) and the Landsat 5 TM absolute calibration error is 7% (Markham and Helder, 2012).

This study did not consider Landsat 5 orbit change impacts on Landsat 5 MSS reflectance. This was because the Landsat 5 local overpass time was relatively stable in the period 1984 to 1992 (due to regular station keeping maneuvers) when the greater majority of Landsat 5 MSS data were acquired. However, given the increasing focus on Landsat time series analyses that include both MSS and TM data (Pflugmacher et al., 2012; Gómez et al., 2011; Fickas et al., 2016; Lobo et al., 2015), caution in the temporal comparison of Landsat 5 TM data acquired from 1995 onward with earlier Landsat 5 MSS data is suggested. Similarly, caution in the comparison of Landsat 5 TM data with Landsat data from other Landsat satellites is suggested. For example, the Global Land Survey (GLS) Landsat data set provides relatively cloud-free single date acquisitions for 1975, 1990, 2000, 2005, and 2010, and includes Landsat 5 TM data for 1990, 2005 and 2010 (Tucker et al., 2004; Gutman et al., 2008).

There are a number of factors that may have influenced the results of this study. First, even for a well maintained satellite orbit, system dependent and independent factors perturb the orbit and so the sensor attitude and position varies (Moreno and Meliá, 1993; Wolfe et al., 2002; Lee et al., 2004). Uncertainties in the position and attitude of the sensor may result in viewing and solar geometry errors (Roy and Singh, 1994). The solar zenith over mountainous terrain may be greater or smaller than for a flat horizontal surface (Teillet et al., 1982) and this is not reflected in the Landsat solar elevation metadata used in this study. However, no definitive Landsat study of these issues has been undertaken, and we did not consider them. Second, the Landsat 5 TM and the MODIS red and NIR bands have slightly different spectral response differences (Steven et al., 2003) but this is unimportant for the main findings of this study as they are based on comparison of the difference between the NBAR derived for the observed and for the reference year 2011 solar zenith angles. Third, the reported statistical fitting error of the 2011 local overpass time model, although low ($r^2 = 0.988$, mean absolute error of 2.34 min) may cause small errors in the reference solar zenith calculation, although the solar zenith angle subtended in a few minutes is typically <0.5°. These errors will have little effect on the reported NBAR reflectance and NDVI ranges and trends because they are calculated based on the relative temporal difference between the NBAR for the observed and 2011 reference solar zenith values and so in two time periods the reference solar zenith angle errors will largely cancel. Fourth, the MODIS BRDF spectral model parameters may not provide a sufficient representation of the surface reflectance anisotropy. The spatial scale dependency of BRDF and its parameterization from remotely sensed observations is an on-going area of research (Widlowski et al., 2001; Pinty et al., 2002; Román et al., 2011). Certainly, there is a significant scale difference between Landsat 30 m and MODIS 500 m pixels and also the CONUS fixed MCD43 500 m spectral BRDF parameter values are smoothed by taking the mean values over twelve months. For these reasons certain geographic locations and times will have greater reflectance anisotropy than captured by the BRDF spectral model parameters and consequently greater Landsat 5 orbit induced reflectance changes than reported in this study.

It is well established that in order to extract information from Landsat time series reliably the data should be pre-processed to remove or minimize remote sensing variations due to non-surface changes, for example, due to factors including sensor degradation and calibration

changes (Markham and Helder, 2012), atmospheric and cloud contamination (Masek et al., 2006), and ideally any data processing issues found in the systematic generation of satellite products (Roy et al., 2002). Further research is recommended to minimize the reflectance impacts of the Landsat 5 orbit changes. One solution is to derive Landsat NBAR for a constant solar zenith angle (Flood et al., 2013), however, semi-empirical BRDF models perform less reliably when used to predict reflectance at solar and view angles that are different to those of the reflectance data used to derive the BRDF model parameters (Lucht and Lewis, 2000). The resulting BRDF solar zenith angle extrapolation errors can be significant given the very large annual variation in Landsat solar zenith observed in this and other studies (Zhang et al., 2016). Another approach suggested by Gao et al. (2014) is to use a pre-existing land cover map and a spatially and temporally explicit look up map of MODIS BRDF parameters indexed by land cover class and NDVI value to normalize BRDF effects. However, this approach is not feasible for global time series application because no multi-temporal 30 m global land cover product exists. Recently, Roy et al. (2016b) found that because the BRDF shapes of different terrestrial surfaces are sufficiently similar over the narrow 15° Landsat field of view, a single fixed set of MODIS BRDF spectral model parameters may be adequate to normalize Landsat view zenith BRDF effects. This NBAR adjustment approach has been implemented using a 2011 solar zenith definition (Zhang et al., 2016) to generate global coverage 30 m Landsat 5 and 7 NBAR surface reflectance data sets that are now available at (http://globalweld.cr.usgs.gov/collections/). Importantly, although the resulting Landsat view zenith NBAR adjustment has little sensitivity to the land cover type, condition, or surface disturbance, and so is suitable for application to the entire Landsat data record, it is *not* recommended for correction of data to a constant solar illumination angle across a wide range of sun angles (Roy et al., 2016b). Further research to develop a Landsat BRDF normalization approach for both view and Landsat 5 orbit drift solar geometry changes is recommended. Meanwhile, users of Landsat 5 TM time series are encouraged to consider the image acquisition solar zenith information with respect to these issues, and pay particular caution when comparing images acquired over anisotropic surfaces that have large solar zenith acquisition differences.

Acknowledgements

This research was funded by the U.S. Department of Interior, U.S. Geological Survey (USGS), under grant G12PC00069 and also by the NASA Making Earth System Data Records for Use in Research Environments (MEaSUREs) program under Cooperative Agreement NNX13AJ24A. The following are thanked for their insightful advice on the history of Landsat 5 orbit maneuvers: Steve Covington (USGS Land Remote Sensing Program Principal Systems Engineer), Sam Goward (University of Maryland), Terry Arvidson (Landsat Senior Systems Engineer), and Darrel Williams (Global Science and Technology Inc.).

References

Arvidson, T., Goward, S., Gasch, J., Williams, D., 2006. Landsat-7 long-term acquisition plan. Photogramm. Eng. Remote. Sens. 72, 1137–1146.
Barnsley, M.J., Allison, D., Lewis, P., 1997. On the information content of multiple-view-angle (MVA) data sets. Int. J. Remote Sens. 18, 1937–1960.
Bhandari, S., Phinn, S., Gill, T., 2012. Preparing Landsat Image Time Series (LITS) for monitoring changes in vegetation phenology in Queensland, Australia. Remote Sens. 4 (6), 1856–1886.
Bindschadler, R., Vornberger, P., Fleming, A., Fox, A., Mullins, J., Binnie, D., Paulsen, S.J., Granneman, B., Gorodetzky, D., 2008. The Landsat image mosaic of Antarctica. Remote Sens. Environ. 112 (12), 4214–4226.
Blanco-Muriel, M., Alarcon-Padilla, D.C., Lopez-Moratalla, T., Lara-Coira, M., 2001. Computing the solar vector. Sol. Energy 70, 431–441.
Boschetti, L., Roy, D.P., Justice, C.O., Humber, M.L., 2015. MODIS-Landsat fusion for large area 30 m burned area mapping. Remote Sens. Environ. 161, 27–42.
Chander, G., Helder, D.L., Malla, R., Micijevic, E., Mettler, C.J., 2007. Consistency of L4 TM absolute calibration with respect to the L5 TM sensor based on near-simultaneous image acquisition. In: Butler, J., Xiong, J. (Eds.), Proceedings of SPIE Conference on Earth Observing Systems XII in San Diego, CA. 6677, p. 66770F.
Chen, J.M., Leblanc, S.G., 2001. Multiple-scattering scheme useful for geometric optical modeling. IEEE Trans. Geosci. Remote Sens. 39 (5), 1061–1071.
Deering, D., Eck, T., Otterman, J., 1990. Bidirectional reflectances of selected desert surfaces and their three-parameter soil characterization. Agric. For. Meteorol. 52 (1–2), 71–93.
Deering, D.W., Middleton, E.M., Eck, T.F., 1994. Reflectance anisotropy for a spruce-hemlock forest canopy. Remote Sens. Environ. 47 (2), 242–260.
Disney, M.I., Lewis, P., Gomez-Dans, J., Roy, D.P., Wooster, M., Lajas, D., 2011. 3D radiative transfer modelling of fire impacts on a two-layer savanna system. Remote Sens. Environ. 115, 1866–1881.
Epiphanio, J.N., Huete, A.R., 1995. Dependence of NDVI and SAVI on sun/sensor geometry and its effect on fAPAR relationships in alfalfa. Remote Sens. Environ. 51 (3), 351–360.
Fensholt, R., Langanke, T., Rasmussen, K., Reenberg, A., Prince, S.D., Tucker, C., Scholes, R.J., Le, Q.B., Bondeau, A., Eastman, R., Epstein, H., 2012. Greenness in semi-arid areas across the globe 1981–2007—an earth observing satellite based analysis of trends and drivers. Remote Sens. Environ. 121, 144–158.
Fickas, K.C., Cohen, W.B., Yang, Z., 2016. Landsat-based monitoring of annual wetland change in the Willamette Valley of Oregon, USA from 1972 to 2012. Wetl. Ecol. Manag. 24 (1), 73–92.
Fisher, J.I., Mustard, J.F., 2007. Cross-scalar satellite phenology from ground, Landsat, and MODIS data. Remote Sens. Environ. 109 (3), 261–273.
Flood, N., Danaher, T., Gill, T., Gillingham, S., 2013. An operational scheme for deriving standardised surface reflectance from Landsat TM/ETM+ and SPOT HRG imagery for Eastern Australia. Remote Sens. 5 (1), 83–109.
Fraser, R.H., Olthof, I., Carrière, M., Deschamps, A., Pouliot, D., 2012. A method for trend-based change analysis in Arctic tundra using the 25-year Landsat archive. Polar Rec. 48 (1), 83–89.
Friedl, M.A., Sulla-Menashe, D., Tan, B., Schneider, A., Ramankutty, N., Sibley, A., Huang, X., 2010. MODIS collection 5 global land cover: algorithm refinements and characterization of new datasets. Remote Sens. Environ. 114, 168–182.
Gao, F., Jin, Y., Schaaf, C.B., Strahler, A.H., 2002. Bidirectional NDVI and atmospherically resistant BRDF inversion for vegetation canopy. IEEE Trans. Geosci. Remote Sens. 40 (6), 1269–1278.
Gao, F., Schaaf, C., Strahler, A., Jin, Y., Li, X., 2003. Detecting vegetation structure using a kernel-based BRDF model. Remote Sens. Environ. 86, 198–205.
Gao, F., He, T., Masek, J.G., Shuai, Y., Schaaf, C.B., Wang, Z., 2014. Angular effects and correction for medium resolution sensors to support crop monitoring. IEEE J. Sel. Top. Appl. Earth Observ. Rem. Sens. 7, 4480–4489.
Gobron, N., Pinty, B., Verstraete, M.M., Govaerts, Y., 1997. A semidiscrete model for the scattering of light by vegetation. J. Geophys. Res.-Atmos. 102, 9431–9446.
Gómez, C., White, J.C., Wulder, M.A., 2011. Characterizing the state and processes of change in a dynamic forest environment using hierarchical spatio-temporal segmentation. Remote Sens. Environ. 115 (7), 1665–1679.
Goward, S.N., Williams, D.L., Irons, J.R., Arvidson, T.J., Rocchio, L.E., Russell, C.A., Johnston, S.S., 2016. Landsat's Enduring Legacy: Pioneering Global Land Observations from Space. American Society of Photogrammetry and Remote Sensing, Bethesda, Maryland (in preparation).
Goward, S.N., Huemmrich, K.F., 1992. Vegetation canopy PAR absorptance and the normalized difference vegetation index: an assessment using the SAIL model. Remote Sens. Environ. 39 (2), 119–140.
Goward, S., Arvidson, T., Williams, D., Faundeen, J., Irons, J., Franks, S., 2006. Historical record of Landsat global coverage: mission operations, NSLRSDA, and international cooperator stations. Photogramm. Eng. Remote. Sens. 72, 1155.
Gray, J., Song, C., 2013. Consistent classification of image time series with automatic adaptive signature generalization. Remote Sens. Environ. 134, 333–341.
Gutman, G., Byrnes, R., Masek, J., Covington, S., Justice, C., Franks, S., Kurtz, R., 2008. Towards monitoring land-cover and land-use changes at a global scale: the Global Land Survey 2005. Photogramm. Eng. Remote. Sens. 74, 6–10.
Hassett, P.J., Johnson, R.L., 1984. LANDSAT-5 orbit adjust maneuver report, NASA contract NAS 5-27888, Task Assignment 14300, Computer Sciences Corp (63.p).
Huete, A.R., 1987. Soil and sun angle interactions on partial canopy spectra. Int. J. Remote Sens. 8 (9), 1307–1317.
Ignatov, A., Laszlo, I., Harrod, E., Kidwell, K., Goodrum, G., 2004. Equator crossing times for NOAA, ERS and EOS sun-synchronous satellites. Int. J. Remote Sens. 25 (23), 5255–5266.
Irish, R.R., Barker, J.L., Goward, S.N., Arvidson, T., 2006. Characterization of the Landsat-7 ETM+ automated cloud-cover assessment (ACCA) algorithm. Photogramm. Eng. Remote. Sens. 72 (10), 1179–1188.
Ishihara, M., Inoue, Y., Ono, K., Shimizu, M., Matsuura, S., 2015. The impact of sunlight conditions on the consistency of vegetation indices in croplands – effective usage of vegetation indices from continuous ground-based spectral measurements. Remote Sens. 7 (10), 14079–14098.
Jackson, R., Teillet, P., Slater, P., Fedosejevs, G., Jasinski, M., Aase, J., Moran, M., 1990. Bidirectional measurements of surface reflectance for view angle corrections of oblique imagery. Remote Sens. Environ. 32, 189–202.
Jacquemoud, S., Verhoef, W., Baret, F., Bacour, C., Zarco-Tejada, P.J., Asner, G.P., Francois, C., Ustin, S.L., 2009. PROSPECT+ SAIL models: a review of use for vegetation characterization. Remote Sens. Environ. 113, S56–S66.
Jönsson, P., Eklundh, L., 2004. TIMESAT—a program for analyzing time-series of satellite sensor data. Comput. Geosci. 30 (8), 833–845.
Ju, J., Masek, J.G., 2016. The vegetation greenness trend in Canada and US Alaska from 1984–2012 Landsat data. Remote Sens. Environ. 176, 1–16.
Ju, J., Roy, D.P., Shuai, Y., Schaaf, C., 2010. Development of an approach for generation of temporally complete daily nadir MODIS reflectance time series. Remote Sens. Environ. 114, 1–20.

Ju, J., Roy, D.P., Vermote, E., Masek, J., Kovalskyy, V., 2012. Continental-scale validation of MODIS-based and LEDAPS Landsat ETM+ atmospheric correction methods. Remote Sens. Environ. 122, 175–184.
Kaufmann, R.K., Zhou, L., Knyazikhin, Y., Shabanov, N.V., Myneni, R.B., Tucker, C.J., 2000. Effect of orbital drift and sensor changes on the time series of AVHRR vegetation index data. IEEE Trans. Geosci. Remote Sens. 38 (6), 2584–2597.
Kovalskyy, V., Roy, D.P., 2013. The global availability of Landsat 5 TM and Landsat 7 ETM+ land surface observations and implications for global 30 m Landsat data product generation. Remote Sens. Environ. 130, 280–293.
Kovalskyy, V., Roy, D.P., Zhang, X.Y., Ju, J., 2012. The suitability of multi-temporal web-enabled Landsat data NDVI for phenological monitoring–a comparison with flux tower and MODIS NDVI. Remote Sens. Lett. 3, 325–334.
Kriebel, K.-T., 1996. On the limited validity of reciprocity in measured BRDFs. Remote Sens. Environ. 58, 52–62.
Leblanc, S.G., Chen, J.M., Cihlar, J., 1997. NDVI directionality in boreal forests: a model interpretation of measurements. Can. J. Remote. Sens. 23 (4), 369–380.
Lee, T., Kaufman, Y.J., 1986. Non-Lambertian effects on remote sensing of surface reflectance and vegetation index. IEEE Trans. Geosci. Remote Sens. GE-24 (5), 699–708.
Lee, D.S., Storey, J.C., Choate, M.J., Hayes, R., 2004. Four years of Landsat-7 on-orbit geometric calibration and performance. IEEE Trans. Geosci. Remote Sens. 42, 2786–2795.
Levi, J.A., Palmer, E., 2011. Strategy for mitigating collisions between Landsat 5 and the afternoon constellation. Proceedings of AAS/AIAA Astrodynamics Specialist Conference, Girdwood, Alaska July 31–August 4, 2011.
Li, X., Strahler, A.H., 1992. Geometric-optical bidirectional reflectance modeling of the discrete crown vegetation canopy: effect of crown shape and mutual shadowing. IEEE Trans. Geosci. Remote Sens. 30, 276–292.
Lobo, F.L., Costa, M.P., Novo, E.M., 2015. Time-series analysis of Landsat-MSS/TM/OLI images over Amazonian waters impacted by gold mining activities. Remote Sens. Environ. 157, 170–184.
Loveland, T.R., Dwyer, J.L., 2012. Landsat: building a strong future. Remote Sens. Environ. 122, 22–29.
Lucht, W., Lewis, P., 2000. Theoretical noise sensitivity of BRDF and albedo retrieval from the EOS-MODIS and MISR sensors with respect to angular sampling. Int. J. Remote Sens. 21 (1), 81–98.
Lucht, W., Schaaf, C.B., Strahler, A.H., 2000. An algorithm for the retrieval of albedo from space using semiempirical BRDF models. IEEE Trans. Geosci. Remote Sens. 38 (2), 977–998.
Markham, B.L., Helder, D.L., 2012. Forty-year calibrated record of earth-reflected radiance from Landsat: a review. Remote Sens. Environ. 122, 30–40.
Masek, J.G., Vermote, E.F., Saleous, N.E., Wolfe, R., Hall, F.G., Huemmrich, K.F., Gao, F., Kutler, J., Lim, T.-K., 2006. A Landsat surface reflectance dataset for North America, 1990–2000. IEEE Geosci. Remote Sens. Lett. 3, 68–72.
McDonald, A.J., Gemmell, F.M., Lewis, P.E., 1998. Investigation of the utility of spectral vegetation indices for determining information on coniferous forests. Remote Sens. Environ. 66 (3), 250–272.
McManus, K.M., Morton, D.C., Masek, J.G., Wang, D., Sexton, J.O., Nagol, J.R., Ropars, P., Boudreau, S., 2012. Satellite-based evidence for shrub and graminoid tundra expansion in northern Quebec from 1986 to 2010. Glob. Chang. Biol. 18, 2313–2323.
Melaas, E.K., Friedl, M.A., Zhu, Z., 2013. Detecting interannual variation in deciduous broadleaf forest phenology using Landsat TM/ETM+ data. Remote Sens. Environ. 132, 176–185.
Moreno, J.F., Meliá, J., 1993. A method for accurate geometric correction of NOAA AVHRR HRPT data. IEEE Trans. Geosci. Remote Sens. 31 (1), 204–226.
Nagol, J.R., Sexton, J.O., Kim, D.-H., Anand, A., Morton, D., Vermote, E., Townshend, J.R., 2015. Bidirectional effects in Landsat reflectance estimates: is there a problem to solve? ISPRS J. Photogramm. Remote Sens. 103, 129–135.
Pflugmacher, D., Cohen, W.B., Kennedy, R.E., 2012. Using Landsat-derived disturbance history (1972–2010) to predict current forest structure. Remote Sens. Environ. 122, 146–165.
Pinter, P.J., 1993. Solar angle independence in the relationship between absorbed PAR and remotely sensed data for alfalfa. Remote Sens. Environ. 46 (1), 19–25.
Pinty, B., Widlowski, J.-L., Gobron, N., Verstraete, M.M., Diner, D.J., 2002. Uniqueness of multiangular measurements. I. An indicator of subpixel surface heterogeneity from MISR. IEEE Trans. Geosci. Remote Sens. 40 (7), 1560–1573.
Privette, J.L., Fowler, C., Wick, G.A., Baldwin, D., Emery, W.J., 1995. Effects of orbital drift on advanced very high resolution radiometer products: normalized difference vegetation index and sea surface temperature. Remote Sens. Environ. 53 (3), 164–171.
Privette, J.L., Eck, T.F., Deering, D.W., 1997. Estimating spectral albedo and nadir reflectance through inversion of simple BRDF models with AVHRR/MODIS-like data. J. Geophys. Res.-Atmos. 102 (D24), 29529–29542.
Rahman, H., Verstraete, M.M., Pinty, B., 1993. Coupled surface-atmosphere reflectance (CSAR) model: 1. Model description and inversion on synthetic data. J. Geophys. Res.-Atmos. 98, 20779–20789.
Roberts, G., 2001. A review of the application of BRDF models to infer land cover parameters at regional and global scales. Prog. Phys. Geogr. 25, 483–511.
Román, M.O., Gatebe, C.K., Schaaf, C.B., Poudyal, R., Wang, Z., King, M.D., 2011. Variability in surface BRDF at different spatial scales (30 m–500 m) over a mixed agricultural landscape as retrieved from airborne and satellite spectral measurements. Remote Sens. Environ. 115 (9), 2184–2203.
Ross, J., 1981. The Radiation Regime and Architecture of Plant Stands. Artech House, Norwood, MA, USA.
Roujean, J.-L., Leroy, M., Deschamps, P.-Y., 1992. A bidirectional reflectance model of the Earth's surface for the correction of remote sensing data. J. Geophys. Res.-Atmos. 97, 20455–20468.
Roy, D.P., Singh, S.M., 1994. The importance of instrument pointing accuracy for surface bidirectional reflectance distribution function mapping. Int. J. Remote Sens. 15 (5), 1091–1099.
Roy, D.P., Borak, J., Devadiga, S., Wolfe, R., Zheng, M., Descloitres, J., 2002. The MODIS land product quality assessment approach. Remote Sens. Environ. 83, 62–76.
Roy, D.P., Ju, J., Kline, K., Scaramuzza, P.L., Kovalskyy, V., Hansen, M., Loveland, T.R., Vermote, E., Zhang, C., 2010. Web-enabled Landsat Data (WELD): Landsat ETM+ composited mosaics of the conterminous United States. Remote Sens. Environ. 114 (1), 35–49.
Roy, D.P., Wulder, M.A., Loveland, T.R., Woodcock, C.E., Allen, R.G., Anderson, M.C., Helder, D., Irons, J.R., Johnson, D.M., Kennedy, R., Scambos, T.A., Schaaf, C.B., Schott, J.R., Sheng, Y., Vermote, E.F., Belward, A.S., Bindschadler, R., Cohen, W.B., Gao, F., Hipple, J.D., Hostert, P., Huntington, J., Justice, C.O., Kilic, A., Kovalskyy, V., Lee, Z.P., Lymburner, L., Masek, J.G., McCorkel, J., Shuai, Y., Trezza, R., Vogelmann, J., Wynne, R.H., Zhu, Z., 2014. Landsat-8: science and product vision for terrestrial global change research. Remote Sens. Environ. 145, 154–172.
Roy, D.P., Kovalskyy, V., Zhang, H.K., Vermote, E.F., Yan, L., Kumar, S.S., Egorov, A., 2016a. Characterization of Landsat-7 to Landsat-8 Reflective Wavelength and Normalized Difference Vegetation Index Continuity. Remote Sens. Environ. 185, 57–70.
Roy, D.P., Zhang, H.K., Ju, J., Gomez-Dans, J.L., Lewis, P.E., Schaaf, C.B., Sun, Q., Li, J., Huang, H., Kovalskyy, V., 2016b. A general method to normalize Landsat reflectance data to nadir BRDF adjusted reflectance. *Remote Sens. Environ.* 176, 255–271.
Schaaf, C.B., Gao, F., Strahler, A.H., Lucht, W., Li, X., Tsang, T., Strugnell, N.C., Zhang, X., Jin, Y., Muller, J.-P., Lewis, P., Barnsley, M., Hobson, P., Disney, M., Roberts, G., Dunderdale, M., Doll, C., d'Entremont, R.P., Hu, B., Liang, S., Privette, J.L., Roy, D.P., 2002. First operational BRDF, albedo nadir reflectance products from MODIS. Remote Sens. Environ. 83, 135–148.
Schaaf, C.L.B., Liu, J., Gao, F., Strahler, A.H., 2011. MODIS albedo and reflectance anisotropy products from Aqua and Terra. In: Ramachandran, B., Justice, C., Abrams, M. (Eds.), Land remote sensing and global environmental change: NASA's Earth observing system and the science of ASTER and MODIS. Remote Sensing and Digital Image Processing Series 11. Springer-Verlag (873 pp.).
Sexton, J.O., Urban, D.L., Donohue, M.J., Song, C., 2013. Long-term land cover dynamics by multi-temporal classification across the Landsat-5 record. Remote Sens. Environ. 128, 246–258. http://dx.doi.org/10.1016/j.rse.2012.10.010.
Snyder, W.C., 1998. Reciprocity of the bidirectional reflectance distribution function (BRDF) in measurements and models of structured surfaces. IEEE Trans. Geosci. Remote Sens. 36, 685–691.
Steven, M.D., Malthus, T.J., Baret, F., Xu, H., Chopping, M.J., 2003. Intercalibration of vegetation indices from different sensor systems. Remote Sens. Environ. 88 (4), 412–422.
Storey, J.C., Choate, M.J., 2004. Landsat-5 bumper-mode geometric correction. IEEE Trans. Geosci. Remote Sens. 42 (12), 2695–2703.
Teillet, P., Guindon, B., Goodenough, D., 1982. On the slope-aspect correction of multispectral scanner data. Can. J. Remote. Sens. 8 (2), 84–106.
Tucker, C.J., Slayback, D.A., Pinzon, J.E., Los, S.O., Myneni, R.B., Taylor, M.G., 2001. Higher northern latitude normalized difference vegetation index and growing season trends from 1982 to 1999. Int. J. Biometeorol. 45 (4), 184–190.
Tucker, C.J., Grant, D.M., Dykstra, J.D., 2004. NASA's global orthorectified Landsat data set. Photogramm. Eng. Remote. Sens. 70, 313–322.
Tucker, C.J., Pinzon, J.E., Brown, M.E., Slayback, D.A., Pak, E.W., Mahoney, R., Vermote, E.F., El Saleous, N., 2005. An extended AVHRR 8-km NDVI dataset compatible with MODIS and SPOT vegetation NDVI data. Int. J. Remote Sens. 26 (20), 4485–4498.
Verbesselt, J., Hyndman, R., Newnham, G., Culvenor, D., 2010. Detecting trend and seasonal changes in satellite image time series. Remote Sens. Environ. 114 (1), 106–115.
Vincent, M.A., 2012. Lessons Learned from the 705-km Fleet, Proceedings of SPIE 8516, Remote Sensing System Engineering IV, 851608, October 2012. http://dx.doi.org/10.1117/12.940771.
Vogelmann, J.E., Xian, G., Homer, C., Tolk, B., 2012. Monitoring gradual ecosystem change using Landsat time series analyses: case studies in selected forest and rangeland ecosystems. Remote Sens. Environ. 122, 92–105.
Vogelmann, J.E., Gallant, A.L., Shi, H., Zhu, Z., 2016. Perspectives on monitoring gradual change across the continuity of Landsat sensors using time-series data. Remote Sens. Environ. 185, 258–270.
Wertz, J.R., 2001. Mission Geometry: Orbit and Constellation Design and Management: Spacecraft Orbit and Attitude Systems. Microcosm Press & Kluwer Academic Publications, The Space Technology Library.
Widlowski, J.L., Pinty, B., Gobron, N., Verstraete, M.M., Davis, A.B., 2001. Characterization of surface heterogeneity detected at the MISR/TERRA subpixel scale. Geophys. Res. Lett. 28 (24), 4639–4642.
Wolfe, R.E., Roy, D.P., Vermote, E., 1998. MODIS land data storage, gridding, and compositing methodology: level 2 grid. IEEE Trans. Geosci. Remote Sens. 36, 1324–1338.
Wolfe, R., Nishihama, M., Fleig, A., Kuyper, J., Roy, D., Storey, J., Patt, F., 2002. Achieving sub-pixel geolocation accuracy in support of MODIS land science. Remote Sens. Environ. 83, 31–49.
Wulder, M.A., White, J.C., Loveland, T.R., Woodcock, C.E., Belward, A.S., Cohen, W.B., Fosnight, G., Shaw, J., Masek, J.G., Roy, D.P., 2016. The global Landsat archive: status, consolidation, and direction. Remote Sens. Environ. 185, 271–283.
Yin, T., Lauret, N., Gastellu-Etchegorry, J.P., 2015. Simulating images of passive sensors with finite field of view by coupling 3-D radiative transfer model and sensor perspective projection. Remote Sens. Environ. 162, 169–185.
Zhang, H.K., Roy, D.P., Kovalskyy, V., 2016. Optimal solar geometry definition for global long term Landsat time series bi-directional reflectance normalization. IEEE Trans. Geosci. Remote Sens. 54 (3), 1410–1418. http://dx.doi.org/10.1109/TGRS.2015.2480684.